



HAL
open science

Robust Fano resonance between mechanical first- and second-order topological states

Linyun Yang, Ying Wu, Kaiping Yu, Rui Zhao, Wei Wang, Bernard Bonello,
Bahram Djafari-Rouhani

► **To cite this version:**

Linyun Yang, Ying Wu, Kaiping Yu, Rui Zhao, Wei Wang, et al.. Robust Fano resonance between mechanical first- and second-order topological states. *International Journal of Mechanical Sciences*, 2022, 236, pp.107768. 10.1016/j.ijmecsci.2022.107768 . hal-03882419

HAL Id: hal-03882419

<https://hal.science/hal-03882419>

Submitted on 2 Dec 2022

HAL is a multi-disciplinary open access archive for the deposit and dissemination of scientific research documents, whether they are published or not. The documents may come from teaching and research institutions in France or abroad, or from public or private research centers.

L'archive ouverte pluridisciplinaire **HAL**, est destinée au dépôt et à la diffusion de documents scientifiques de niveau recherche, publiés ou non, émanant des établissements d'enseignement et de recherche français ou étrangers, des laboratoires publics ou privés.

Journal Pre-proof

Robust Fano resonance between mechanical first- and second-order topological states

Linyun Yang, Ying Wu, Kaiping Yu, Rui Zhao, Wei Wang,
Bernard Bonello, Bahram Djafari-Rouhani



PII: S0020-7403(22)00648-8

DOI: <https://doi.org/10.1016/j.ijmecsci.2022.107768>

Reference: MS 107768

To appear in: *International Journal of Mechanical Sciences*

Received date: 29 June 2022

Revised date: 17 September 2022

Accepted date: 18 September 2022

Please cite this article as: L. Yang, Y. Wu, K. Yu et al., Robust Fano resonance between mechanical first- and second-order topological states. *International Journal of Mechanical Sciences* (2022), doi: <https://doi.org/10.1016/j.ijmecsci.2022.107768>.

This is a PDF file of an article that has undergone enhancements after acceptance, such as the addition of a cover page and metadata, and formatting for readability, but it is not yet the definitive version of record. This version will undergo additional copyediting, typesetting and review before it is published in its final form, but we are providing this version to give early visibility of the article. Please note that, during the production process, errors may be discovered which could affect the content, and all legal disclaimers that apply to the journal pertain.

© 2022 Published by Elsevier Ltd.

Robust Fano resonance between mechanical first- and second-order topological states

Linyun Yang^a, Ying Wu^{b,*}, Kaiping Yu^{a,**}, Rui Zhao^a, Wei Wang^c, Bernard Bonello^d,
Bahram Djafari-Rouhani^e

^a*Department of Astronautic Science and Mechanics, Harbin Institute of Technology, Harbin, Heilongjiang 150001, China*

^b*School of Science, Nanjing University of Science and Technology, Nanjing, 210094, China*

^c*Department of Physics, Hong Kong Baptist University, Kowloon Tong, Hong Kong, China*

^d*Sorbonne Université, UPMC Université Paris 06 (INSP-UMR CNRS 7588), 4, place Jussieu 75005 Paris, France*

^e*Institut d'Electronique, de Microélectronique et de Nanotechnologie, UMR CNRS 8520, Département de Physique, Université de Lille, 59650 Villeneuve d'Ascq, France*

Abstract

The Fano resonance, as a phenomenon of wave scattering, is based on the interaction between a “bright mode” and a “dark mode” giving rise to an asymmetric and ultrasharp spectral peak. However, the Fano resonant frequency is sensitive to structural imperfections such as defects or disorders, which will shift the resonant peak, or even damage the Fano line shape. Here, we harness the coupling between the first-order and the higher-order topological insulators to overcome this shortcoming. We construct a first-order topological edge state to serve as a bright mode, and a second-order topological corner state to be the dark mode using the same base configuration. As a result, a topological Fano resonance is expected to occur around the resonant frequency of the dark mode. The robustness of the Fano resonance is verified by deliberately introducing various types of imperfections into the system. Our findings may further enhance confidence in using the resonance such as acoustic switching, refractive index sensing, high quality factor filters, and accurate interferometers.

Keywords: Topological edge states, second order corner modes, Fano resonance, ultrahigh Q factor

*Corresponding author

**Corresponding author

Email addresses: wuyinghit@gmail.com (Ying Wu), yukp@hit.edu.cn (Kaiping Yu)

Contents

1	Introduction	3
2	The bulk band structure and topology of the phononic plate	5
3	The first-order topological edge states	14
4	The second-order topological corner states	15
5	Occurrence of topological Fano resonance	17
6	Robustness of topological Fano resonance	21
7	Discussions and Conclusions	23
Appendix A	Symmetry reconstruction of degenerate eigenmodes	24
Appendix B	The effective Hamiltonian by $k \cdot p$ method	26
Appendix C	The frequency responses for topological edge states	30
Appendix D	Comparison between the topological corner and trivial cavity modes	31
Appendix E	The multiple scattering method for flexural wave in thin plates	32
Appendix F	Double asymmetric Fano profiles by two different waveguide-corner coupling strengths	33
Appendix G	The loss effects on the Fano resonance	35

1. Introduction

Fano resonance, originally discovered in quantum systems, is a wave scattering phenomenon featuring asymmetric and ultra-sharp spectral peaks resulting from the interference between discrete and continuum scattering channels. It is named after Ugo Fano, for his contribution to the theoretical explanation for the scattering line shape of inelastic scattering between electrons and helium atoms[1]. The wave interference is not exclusive of quantum mechanics, while it is a general wave phenomenon and the occurrence of Fano resonance has been evidenced in other fields such as photonic crystals [2, 3], plasmonic nanostructures [4, 5] and phononic crystals [6]. Two ingredients, including a broadband “bright” mode serving as a background state and a narrowband “dark” mode as an isolated state, are essential for the generation of Fano resonance in classical systems [7]. Around the dark mode resonant frequency, the bright mode magnitude varies slowly with frequency, while the dark mode changes abruptly both in magnitude and phase. When the driven force passes through the resonant frequency, both the in-phase and out-of-phase interactions between the two modes will take place within a very narrowband range. As a result, the constructive and destructive interferences enable the transmittance to reach its maximum from the minimum very quickly, which creates the asymmetric Fano-like profile.

Based on such a straightforward formulation, advances in theoretical and experimental demonstrations of Fano resonance have been achieved in mechanical and acoustic systems [6, 8–14]. Because of the asymmetric and ultra-sharp properties, Fano resonances in phononic crystals possess a variety of potential applications such as acoustic switching, refractive index sensing, high-quality factor filters, and highly accurate interferometers. While the high sensitivity of the Fano resonance requires precise control and accurate fabrication [15]. Additionally, structural imperfections such as defects or disorder may shift the Fano resonant frequency, or even completely damage the Fano line shape. The developments of topological insulators (TIs) [16, 17] and their classical analog in optical [18–21], acoustical [22–28] and mechanical [29–40] systems may provide an elegant solution to this problem. TIs support unique edge states protected by the intrinsic bulk bands topology, regardless of the local perturbations such as defects or disorders. Inspired by this preeminent feature, the ultra-sharp spectrum of Fano resonances can be guaranteed by topological protection in 1D acoustic/mechanical systems [15, 41]. In 2D systems, a topological waveguide and a trivial cavity are proposed to serve as the bright and dark modes, respectively [42–44]. By placing a care-

fully designed cavity besides the topological waveguide, a coupler can be constructed to support both constructive and destructive interferences between the two modes, which creates a topological Fano resonance. However, only the robustness of the bright mode is guaranteed by the topological protection, while the dark mode, i.e., the cavity mode, still remains trivial and less robust.

Here, we harness the very recently discovered higher-order topological insulators (HOTIs) [45–59] to achieve a robust dark mode. Generally speaking, an n -order topological insulator in a d -dimensional system can support $(d - n)$ dimensional topological states, where the order $n \geq 2$ indicates a higher-order topology, while $n = 1$ refers to the conventional TIs [60]. Unlike the conventional TIs with edge states, which has one lower dimension than that of the bulk, the HOTIs host topological corner states whose dimension is at least two less than the bulk. Hence, we replace

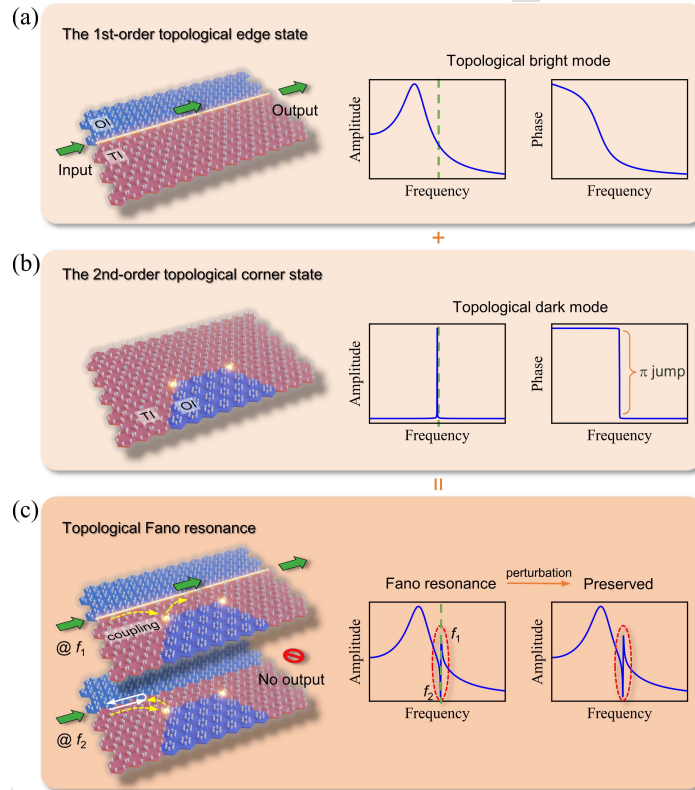


Figure 1: **Illustration of the occurrence of topological Fano resonance.** (a) The schematic view of the 1st-order topological edge state and its transmission spectrum, (b) The 2nd-order topological corner state and its transmission spectrum, (c) the robust topological Fano resonance and its ultra-sharp and antisymmetric transmission line resulted from the coupling between the topological edge and corner states.

the trivial cavity by the second-order topological insulators (SOTIs), which supports topologically protected 0D corner states. By integrating the 0D topological corner state and the 1D edge state in a properly designed 2D phononic crystal structure, we realize a topological Fano resonance with both topologically protected bright and dark modes. Specifically, as conceptually depicted in Fig. 1, we construct a first-order topological edge state to serve as a bright mode [Fig. 1(a)], and a second-order topological corner state to be the dark mode [Fig. 1(b)]. The coupling of these two modes can be achieved by a proper arrangement of regions occupied by the topological insulator (TI) and the ordinary insulator (OI). As a result, a topological Fano resonance can be expected to occur around the resonant frequency of the dark mode, as shown in Fig. 1(c).

The arrangement of the rest of this paper is outlined as follows: In Sec. 2, we introduce a phononic crystal plate with breathing honeycomb unit cells, and show that the shrunken (type A) and expanded (type B) lattices belong to distinct topological phases. In Sec. 3, we demonstrate the existence of the first-order topological edge states confined at the domain wall formed by different topological structures. We then show that these two edge states are in fact not gapless, furthermore, the edge state gap can be tuned by alternating the geometrical parameters. This is followed by Sec. 4 in which we illustrate the second-order topological corner states that reside within the edge state gap. In Sec. 5, we propose a compound lattice structure with two types of domain walls that respectively supports topological edge states as well as the in-gap topological corner states at a common frequency. We show that within an extremely narrow range around this specific frequency, the topological edge and corner modes will undergo both constructive and destructive interferences, resulting to an asymmetric and ultra-sharp transmission line, i.e., a Fano-like resonance. We further illustrate in Sec. 6 that the topological Fano shape response can be preserved and the resonance frequency shift is very small at the presence of various geometrical imperfections, including random rotations or deformations. Finally, we summarize the main results of this paper in Sec. 7.

2. The bulk band structure and topology of the phononic plate

We consider the flexural wave propagation problem in a thin elastic plate attached by mass-spring oscillators with a honeycomb arrangement as depicted in Fig. 2(a) and (b). The yellow background and the white circles represent the homogeneous plate and the periodic oscillators, respectively. Each unit cell comprises six identical resonators located at the vertices of a hexagon with

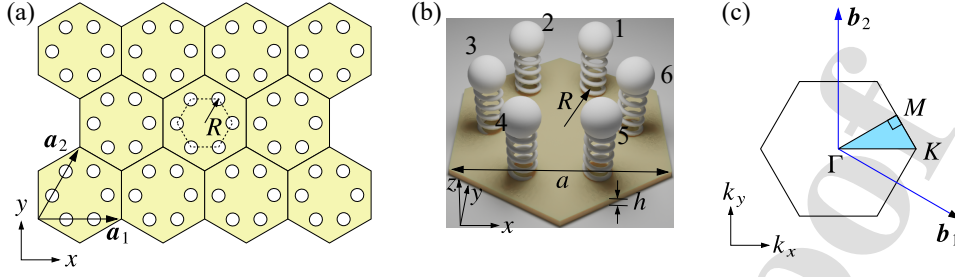


Figure 2: **Schematic view of the phononic plate.** (a) Top view of the phononic plate in the xy plane, each white circle represents one oscillator. (b) The perspective view of one unit cell. (c) The first Brillouin zone of the honeycomb lattice.

side length R , while the lattice constant is denoted by a . The phononic crystal plate is created by periodically repeating one unit cell along the lattice vectors $\mathbf{a}_1 = a(1, 0)$ and $\mathbf{a}_2 = a(1/2, \sqrt{3}/2)$. The first Brillouin zone and the reciprocal lattice vectors $\mathbf{b}_1 = 2\pi/a(1, -1/\sqrt{3})$ and $\mathbf{b}_2 = 2\pi/a(0, 2/\sqrt{3})$, which satisfy the relation $\mathbf{a}_i \cdot \mathbf{b}_j = 2\pi\delta_{ij}$, are displayed in Fig. 2(c).

For a specific geometrical configuration that $R = a/3$ (denoted by R_0), the lattice sustains a fourfold degeneracy in the dispersion curves and a double Dirac cone occurs at the Brillouin zone center due to the zone-folding mechanism [20]. By varying the ratio between R and a , the switching between distinct topological phases can be achieved. Briefly speaking, for a shrunken cell, i.e., $R/a < 1/3$, the corresponding band gap features a topologically trivial phase, while for an expanded cell that $R/a > 1/3$, it is topologically nontrivial [20, 50], as we will describe below later. It is worth noting that the above scheme to create topologically distinct phases was widely used to achieve TIs by mimicking the quantum spin Hall effect [20, 25, 31, 61, 62] or to realize recently proposed SOTIs [50, 52, 57, 63] in classical wave systems. Here we adopt this mechanism to realize both the topological edge and corner states simultaneously at the same frequency, and investigate their coupling effects and the resultant topologically protected robust Fano resonance.

2.1. Weak form for elastic wave equations in periodic systems

Weak forms are powerful mathematical tools to solve partial differential equations (PDEs), especially in finite element formulations. To obtain the band structure and to discuss its bulk topology of the proposed phononic crystal plate, we first deduce the weak form formulation for three-dimensional elastodynamic equations in periodic systems. Its implementations to the flexural wave problems in phononic plate structures will be discussed in the next section.

For elastic waves in homogeneous and linear elastic materials, the equations of motion without body forces expressed in terms of components with respect to a Cartesian coordinate system (x, y, z) are

$$\sigma_{ij,j} - \rho \ddot{u}_i = 0 \quad (1)$$

where ρ is the mass density, σ_{ij} and u_i ($i, j = x, y, z$) denote respectively the Cauchy stress tensor and the displacement vector components, and \ddot{u}_i represents the second derivative of u_i with respect to time. Note that the comma in the subscript denotes partial differentiation, and that the summation convention over a repeated subscript is adopted.

The Cauchy stress tensor σ and the infinitesimal strain tensor ε are related by the constitutive equations, or known as Hooke's law,

$$\sigma_{ij} = C_{ijkl} \varepsilon_{kl} \quad (2)$$

where C_{ijkl} is the four-order stiffness tensor, and the strain-displacement equations are

$$\varepsilon_{ij} = \frac{1}{2}(u_{i,j} + u_{j,i}) \quad (3)$$

The weak form for Eq. (1) can be derived by multiplying itself by a test function using variation notation δu_i , and then integrating the result over the solution domain Ω [64]. The terms with derivatives of stresses are treated by integrating by parts using Green's theorem, which yields

$$\int_{\Omega} [\rho \delta u_i \ddot{u}_i + \delta u_{i,j} \sigma_{ij}] dV - \int_{\partial\Omega} \delta u_i \cdot \sigma_{ij} n_j dS = 0 \quad (4)$$

where $\partial\Omega = \partial\Omega_u \cup \partial\Omega_t$ denotes the boundary surface with the subscripts u and t refer to the boundaries with prescribed displacements and tractions respectively, n_j is the j -th component of the normal vector. The boundary integration term can be simplified by removing the essential boundary condition part since $\delta u_i = 0$ is valid on $\partial\Omega_u$, and preserving only the natural boundary condition part which is $\sigma_{ij} n_j = f_i$ with f_i being the known traction on $\partial\Omega_t$.

According to the Bloch theorem, the displacement field $u_i = u_i(x, y, z)$ in periodic structures with lattice vectors \mathbf{a}_i has the following form

$$u_i = \hat{u}_i \exp(ik_i x_i) \quad (5)$$

where k_i is the wave vector component, \hat{u}_i is the cell-periodic counterpart of the Bloch wave u_i , which has the same periodicity with the unit cell. We stress that the repeated subscript implies the

summation convention. From Eq. (5), the derivatives of the displacement field can be expressed as

$$u_{i,j} = (\hat{u}_{i,j} + ik_j \hat{u}_i) \exp(ik_l x_l) \quad (6)$$

Consequently, the variation term δu_i in Eq. (4) should be replaced by its complex conjugation δu_i^* , since the integration represents an inner product operation. Inserting Eq. (6) back into Eqs. (2) – (3), it can be seen that the stress and strain tensors are also Bloch functions, i.e., they have similar expressions to Eq. (5),

$$\sigma_{ij} = \hat{\sigma}_{ij} \exp(ik_l x_l) \quad (7a)$$

$$\varepsilon_{ij} = \hat{\varepsilon}_{ij} \exp(ik_l x_l) \quad (7b)$$

where $\hat{\varepsilon}_{ij} = \frac{1}{2}[(\hat{u}_{i,j} + ik_j \hat{u}_i) + (\hat{u}_{j,i} + ik_i \hat{u}_j)]$, and $\hat{\sigma}_{ij} = C_{ijkl} \hat{\varepsilon}_{kl}$. Now inserting Eqs. (5) – (7) back into Eq. (4) yields the weak form for wave equations in periodic structures as

$$\int_{\Omega} [\rho \delta \hat{u}_i^* \ddot{\hat{u}}_i + \delta(\hat{\varepsilon}_{ij}^*) \hat{\sigma}_{ij}] dV - \int_{\partial\Omega} \delta \hat{u}_i^* \cdot \hat{f}_i dS = 0 \quad (8)$$

in which the identity $\delta u_{i,j} \sigma_{ij} = \delta(\varepsilon_{ij}) \sigma_{ij}$ is used with the symmetry nature of the stress tensor being taken into consideration. We stress again that δu_i and $\delta u_{i,j}$ have been replaced by their complex conjugations as required by the complex-valued inner product, and that an auxiliary function $\hat{f}_i = f_i \exp(-ik_l x_l)$ where $f_i = \sigma_{ij} n_j$ is introduced to make the expression of Eq. (8) remain compact.

The weak form Eq. (8) is applicable for Bloch modes in general 3D periodic solid materials, which can be solved efficiently by using the weak form PDE module of COMSOL Multiphysics, combined with periodic boundary conditions imposed on \hat{u}_i . Moreover, when considering the flexural waves in elastic plates whose thickness h is very small compared with the other two dimensions, additional assumptions regarding the behavior of such structures such as the Kirchhoff theory for thin plates or the Reissner-Mindlin theory for thick plates, can further reduce the formulation from complete three- to two-dimensional equations.

2.2. Weak form for flexural wave in phononic plates

In thin plate theory, the deformation is represented by a single variable w , the out-of-plane displacement of the mid-plane of the plate. This displacement is governed by a four-order PDE according to Kirchhoff's assumption, which introduces second derivatives of w in the expressions

of strains. However, the requirement that both w and its derivatives need to be continuous brings more difficulties in the finite element formulations. In contrast, it turns out that the thick plate theory is simpler to implement in the finite element analysis, since only up to the first derivatives of the dependent variables appear in the strain terms. According to the Reissner-Mindlin plate theory, in which the transverse shear and rotary inertia are taken into consideration, the displacement components for flexural motions are expressed in the forms [65]

$$u(x, y, z) = -z\theta_x(x, y) \quad (9a)$$

$$v(x, y, z) = -z\theta_y(x, y) \quad (9b)$$

$$w(x, y, z) = w(x, y) \quad (9c)$$

where θ_x and θ_y are the local rotations of the normal to the mid-plane of the plate, with respect to the x and y axis, respectively. The strains now can be separated into bending and transverse shear parts as follows

$$\varepsilon_{xx} = -z\theta_{x,x}, \quad \varepsilon_{yy} = -z\theta_{y,y}, \quad \varepsilon_{xy} = -\frac{z}{2}(\theta_{x,y} + \theta_{y,x}) \quad (10a)$$

$$\varepsilon_{xz} = \frac{1}{2}(-\theta_x + w_{,x}), \quad \varepsilon_{yz} = \frac{1}{2}(-\theta_y + w_{,y}) \quad (10b)$$

Note that the comma in the subscript implies partial differentiation. The flexural motions of the plate can be approximately regarded as a plane stress condition, thus the stresses corresponding to the strains above are

$$\sigma_{xx} = \frac{E}{1-\nu^2}(\varepsilon_{xx} + \nu\varepsilon_{yy}) \quad (11a)$$

$$\sigma_{yy} = \frac{E}{1-\nu^2}(\varepsilon_{yy} + \nu\varepsilon_{xx}) \quad (11b)$$

$$\sigma_{ij} = \mu\varepsilon_{ij} \quad (i \neq j \text{ and } i, j = x, y, z) \quad (11c)$$

where E , μ and ν are the Young's modulus, shear modulus and Poisson's ratio of the isotropic plate material. Considering that the flexural wave propagates in the xy plane, the out-of-plane component of the wave vector should be zero, i.e., $k_z = 0$, while the other two are retained. Therefore, according to Eq. (5) for the Bloch waves in three dimensions, the displacements in Eq. (9) can also be expressed in a similar manner, for example, $u = -z\hat{\theta}_x \exp(ik_x x + ik_y y)$ with $\hat{\theta}_x(x, y)$ a periodic function. Finally, substituting Eqs. (9) – (11) into Eq. (8), and analytically performing the

through-thickness integration yields

$$\int_A \left\{ \frac{1}{12} \rho h^3 (\delta \hat{\theta}_x^* \ddot{\theta}_x + \delta \hat{\theta}_y^* \ddot{\theta}_y) + \rho h \delta \hat{w}^* \ddot{w} \right. \\ \left. + \frac{1}{12} h^3 [\delta (\hat{\varepsilon}_{xx}^{(0)*}) \hat{\sigma}_{xx}^{(0)} + \delta (\hat{\varepsilon}_{yy}^{(0)*}) \hat{\sigma}_{yy}^{(0)} + 2\delta (\hat{\varepsilon}_{xy}^{(0)*}) \hat{\sigma}_{xy}^{(0)}] \right. \\ \left. + 2\gamma h [\delta (\hat{\varepsilon}_{xz}^{(0)*}) \hat{\sigma}_{xz}^{(0)} + \delta (\hat{\varepsilon}_{yz}^{(0)*}) \hat{\sigma}_{yz}^{(0)}] - \delta \hat{w}^* \hat{f}_z \right\} dA = 0 \quad (12)$$

where A denotes the two-dimensional region of one unit cell, $\gamma = \pi^2/12$ is the correction factor introduced to account for the fact that the shear stresses are not constant over the thickness [65], h is the plate thickness, and the strain and stress terms with superscript $\cdot^{(0)}$ represent their z -independent parts. The strain terms are given by

$$\hat{\varepsilon}_{xx}^{(0)} = \hat{\theta}_{x,x} + ik_x \hat{\theta}_x, \quad \hat{\varepsilon}_{yy}^{(0)} = \hat{\theta}_{y,y} + ik_y \hat{\theta}_y, \quad \hat{\varepsilon}_{xy}^{(0)} = \frac{1}{2} (\hat{\theta}_{x,y} + ik_y \hat{\theta}_x + \hat{\theta}_{y,x} + ik_x \hat{\theta}_y) \quad (13a)$$

$$\hat{\varepsilon}_{xz}^{(0)} = \frac{1}{2} (-\hat{\theta}_x + \hat{w}_{,x} + ik_x \hat{w}), \quad \hat{\varepsilon}_{yz}^{(0)} = \frac{1}{2} (-\hat{\theta}_y + \hat{w}_{,y} + ik_y \hat{w}) \quad (13b)$$

and the stress terms can be subsequently obtained from Eq. (11).

The weak form formulation Eq. (12) is deduced from the weak form of 3D elastodynamic wave equations, with specific assumptions made on the displacement fields to describe the flexural motions of thick plates. Considering the periodicity of phononic crystal plates, the displacements are further regarded as Bloch waves, resulting in the emergence of their cell-periodic counterparts and the wave vector (k_x, k_y) in the weak form expression. In this paper, Eq. (12) is solved for various wave vectors by using the weak form PDE module of the finite element software COMSOL Multiphysics with the eigenvalue solver in two dimensions. Then the dispersion curves can be obtained from the eigenfrequencies solutions. It is worth noting that the surface traction in the last term can be determined by the reaction forces from the oscillators as will be detailed below.

2.3. The band structure and the topological phase transition

Consider the phononic crystal plate shown in Fig. 2, with lattice constant $a = 50$ mm, thickness $h = 0.5$ mm and the material constants Young's modulus $E = 70$ GPa, Poisson's ration $\nu = 0.3$ and mass density $\rho = 2700$ kg/m³. We assume that each oscillator has only one degree of freedom, the vertical displacement parallel to the z axis. The time-harmonic vibration of the resonators interacts with the elastic plate through the connecting springs, which gives the reaction force as [39]

$$f_z(\mathbf{r}) = \sum_{\alpha=1}^6 m_{\alpha} \frac{\omega_{\alpha}^2 \omega^2}{\omega_{\alpha}^2 - \omega^2} w(\mathbf{R}_{\alpha}) \delta(\mathbf{r} - \mathbf{R}_{\alpha}) \quad (14)$$

where $m_{\alpha}, \kappa_{\alpha}$ and $\omega_{\alpha} = \sqrt{\kappa_{\alpha}/m_{\alpha}}$ are respectively the mass, spring constant and the resonant frequency of oscillator α , which locates at \mathbf{R}_{α} . $\delta(\mathbf{r})$ denotes the Dirac delta function.

For simplification we also assume that the resonant frequencies of the oscillators are sufficiently higher than the working frequency we are interested in, with the limiting case being that the masses are rigidly connected to the plate surface. In other words, we let the spring constant $\kappa_{\alpha} \rightarrow +\infty$ and set the mass to be a finite value, for example $m_{\alpha} = 5\rho a^2 h$. Consequently, the force term Eq. (14) can be further simplified as

$$f_z(\mathbf{r}) = \sum_{\alpha} m_{\alpha} \omega^2 w(\mathbf{r}_{\alpha}) \delta(\mathbf{r} - \mathbf{R}_{\alpha}) \quad (15)$$

This treatment can keep our physical model rather simple without introducing additional resonant features, and in the meantime, it does not affect the demonstration of the topological Fano resonance phenomenon or the physical mechanism behind it.

We first consider the geometrical configuration for $R/R_0 = 1$ (notice that $R_0 = a/3$), which corresponds to a perfect honeycomb lattice, or a phononic analog of graphene. In this scenario, the primitive unit cell (i.e., the smallest one) consists of only two oscillators, while the unit cell shown in Fig. 2(b) is in fact a supercell. This specific selection of an enlarged unit cell allows the formation of a double Dirac cone at Γ point due to a band folding mechanism. By solving Eq. (12), the gapless band diagram for $R = R_0$ shown in Fig. 3(a) unambiguously reveals the occurrence of a double Dirac cone at 331.7 Hz, which is again confirmed by the theoretically predicted results by $\mathbf{k} \cdot \mathbf{p}$ method (blue solid lines) which show a very good correspondence with the finite element method (FEM) results (white open circles). For the details of the implementation of $\mathbf{k} \cdot \mathbf{p}$ method, please refer to Appendix B. The right panel shows the field distributions of the four-fold degenerate modes, which are denoted by $p_x, p_y, d_{x^2-y^2}$ and d_{xy} according to their symmetries. For example, the dipole-like modes $p_{x(y)}$ are antisymmetric about the $x(y)$ axis, but symmetric about the $y(x)$ axis. While the quadruple-like modes $d_{x^2-y^2}(d_{xy})$ are symmetric (antisymmetric) about both x and y axes. Besides the mirror symmetries, under a \hat{r}_2 operation (180° rotation), the p -modes will flip their sign while the d -modes remain unchanged. It is worth noting that these four degenerate modes are generally hybridized in numerical calculations and therefore the aforementioned symmetries

are usually broken and thus may need to be constructed by a combination of the degenerate eigenmodes. To overcome this shortcoming, we present a scheme based on projection (see Appendix A) to reconstruct the mode symmetries. We have also presented the phase map of these eigenmodes in Fig. A.10 for a better visualization of the rotational eigenvalue of them.

For values of $R \neq R_0$, the translational symmetry of the above two-resonator “primitive cell” is broken, and thus the band folding mechanism is no longer applicable, which breaks the four-fold degeneracy and opens a complete band gap between the two-fold p modes and d modes. Fig. 3(b) presents the varying of the upper and lower gap limits when R/R_0 takes different values. Starting from $R/R_0 = 0.7$, as we increase the value of R/R_0 , the band gap decreases gradually and closes

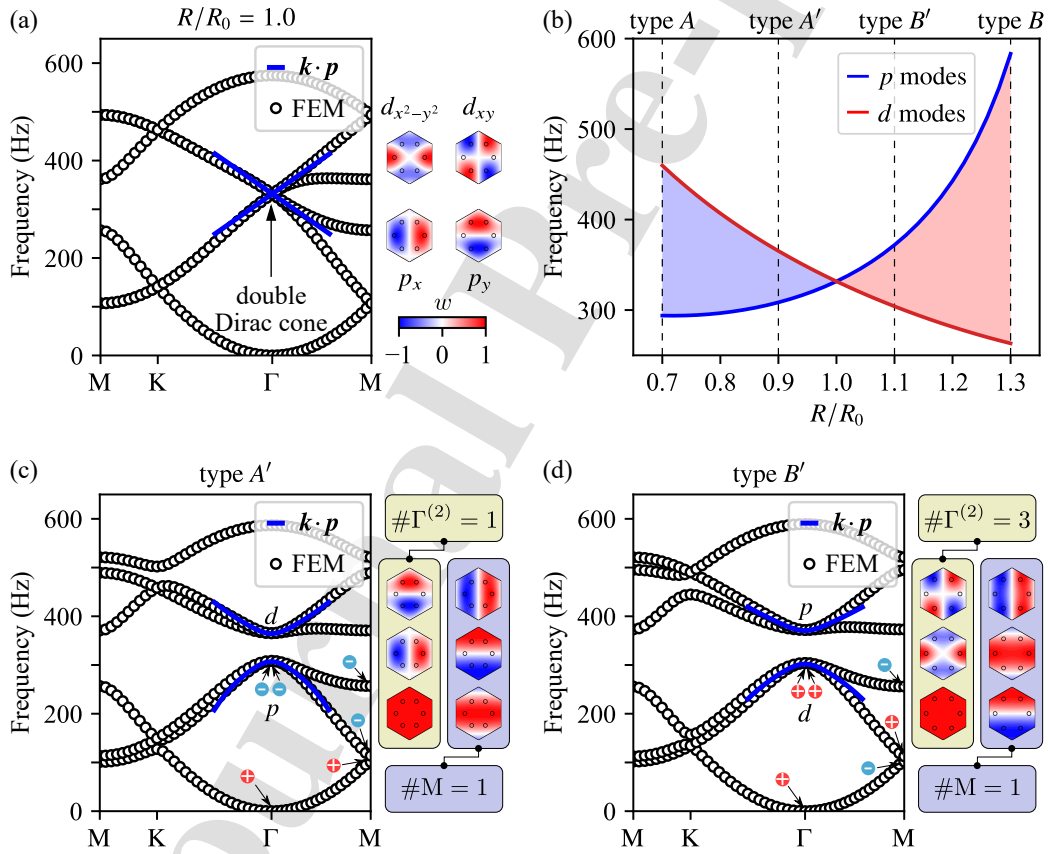


Figure 3: **Bulk band structures and the topological transition.** The band diagram for the critical configuration when $R_1 = R_0$, where a double Dirac cone is formed. The open circles refer to the FEM simulations whereas blue curves are the results of $k \cdot p$ theory (see Appendix B). The eigenvectors at the Γ point are shown on the right. (b) the topological phase transition as R_1 varies revealed by the lifting of the Dirac cone degeneracy. (c) and (d) the band structures and eigenmodes at Γ and M point for configuration A' and B' , respectively.

when reaching at the critical point $R/R_0 = 1$. If R/R_0 is further increased, the band gap will reopen again but with the eigenmodes switched their orders, i.e., the p modes correspond to the two bands above the gap while the d modes correspond to the two below. Such a band inversion is often accompanied by a topological transition from a trivial phase to a nontrivial one. In the case for time reversal symmetry preserved C_{6v} breathing lattices, for values of $R/R_0 < 1$ the band gap is topologically trivial and for those $R/R_0 > 1$ it is nontrivial [20, 50]. This can be explained by checking the (pseudo) spin Chern numbers based on an effective Hamiltonian obtained by $\mathbf{k} \cdot \mathbf{p}$ method (see Appendix B). To have a deeper understanding of these two topologically distinct phases, we plot the band structures of two example cases for $R/R_0 = 0.9$ (lattice A') and $R/R_0 = 1.1$ (lattice B') in Fig. 3(c) and (d). Good agreements between the $\mathbf{k} \cdot \mathbf{p}$ predictions and the first principle FEM results can be found around Γ point for bands 2 – 5, indicating that we can use an effective Hamiltonian to describe the band structure and its topological properties. Besides, there are 3 bands below the complete band gap, and their corresponding eigenmodes at Γ and M points are displayed in the right panels of each figure. The sign + (or –) marked in the band diagrams indicates that the corresponding eigenmode has an even (or odd) C_2 rotation symmetry, and $\#\Gamma^{(2)}$ ($\#M$) is the number of eigenmodes that have C_2 rotation eigenvalue +1 at Γ (M) points for all the bands below the gap. Based on these two integer numbers, the C_2 topological invariant is defined as [50, 51]

$$[M] = \#M - \#\Gamma^{(2)} \quad (16)$$

which is a measure of the difference between the subspaces spanned by the bands below the gap at M and Γ points in the C_2 representation. Besides, a C_3 topological invariant can also be defined in a similar manner as $[K] = \#K - \#\Gamma^{(3)}$, where $\#K$ and $\Gamma^{(3)}$ are the number of eigenmodes below the gap that have C_3 rotation eigenvalue +1 for K and Γ points, respectively. Therefore, the bulk topology of the band gap can be characterized by [50, 51]

$$\chi = ([M], [K]) \quad (17)$$

For example, a zero-valued χ implies that the \mathbf{k} -dependent Hamiltonian can be continuously deformed along the path that joins the high symmetric points M (or K) and Γ without closing the band gap or breaking the symmetry, rendering the bulk topology trivial [50]. In contrast, $\chi \neq (0, 0)$ reveals a nontrivial topology because the low-frequency subspaces below the gap at these points are

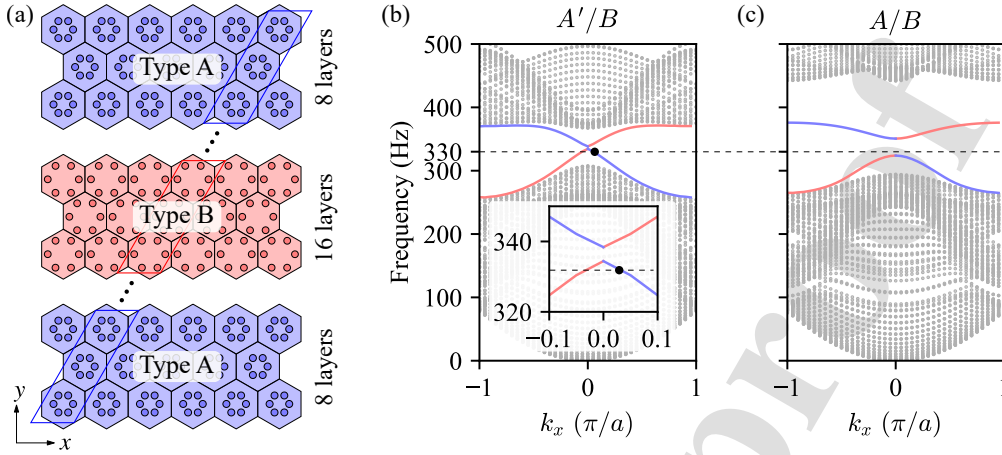


Figure 4: **The first-order topological edge states.** (a) Schematic view of a ribbon consisting of 16 layers of lattice B sandwiched in between 8 layers of lattice A (or A') on both sides. The band structures for (b) A'/B and (c) A/B interfaces along the k_x direction. The inset in (b) shows a zoom in view near the tiny topological edge band gap.

non-equivalent. In our case, by checking the parities of the eigenmodes at M and Γ points shown in Fig. 3(c) and (d), we can obtain $[M] = 0$ for the configuration that $R < R_0$ while $[M] = -2$ for $R > R_0$. As for the C_3 invariant, $[K] = 0$ is valid for all ratios of R/R_0 in our system. This indicates that the configuration that $R > R_0$ is in a nontrivial phase with $\chi = (-2, 0) \neq (0, 0)$ and consequently one can expect the observation of corner modes localized at the intersections of topological domain walls [50].

3. The first-order topological edge states

According to the bulk-edge correspondence, it is known that there exist a pair of topological edge states confined at the domain wall formed by the two topologically distinct lattices. As shown in Fig. 4(a), we calculate the band structure of a supercell consisting of 16 layers of lattice B sandwiched in between 8 layers of lattice A (or A') on each side, by applying periodic boundary conditions on both the left-right and top-bottom edge pairs. Note that the top and bottom termination can be viewed as they were sutured together due to the periodic boundary condition, which eliminates the boundary modes and allows us to focus on the edge states confined at the domain walls.

Let us first consider the edge states confined at A'/B interface, as shown in Fig. 4(b). Clearly,

two branches of bands (red and blue solid lines) emerge in the common frequency range of the bulk band gaps of lattices A' and B . Moreover, the corresponding eigenmodes of these two bands feature very localized amplitude-distributions near the topological domain walls (not shown). However, we would like to mention that these two edge states are not gapless, and that there exists a tiny gap between them. The reason is that the C_6 symmetry of the entire structure is not strictly preserved due to the deviations between lattices at different sides of the domain wall [31]. It can be expected that this tiny gap could even be extended to be sufficiently large if the configuration difference between the two lattices is further enlarged. This is indeed the case for the result shown in Fig. 4(c), where the lattice A' , with geometrical configuration $R/R_0 = 0.9$, has been replaced by lattice A which has a smaller value of $R/R_0 (= 0.7)$. Compared with Fig. 4(b), it is much more obvious that there exists a band gap in between the blue and red branches of edge states, making the topological edge states gapped themselves. One may notice that there is another band gap between the upper branch of topological edge state and the bulk states, but the second order topological corner modes are expected to reside inside the band gap of the first order topological edge states. We will show later that the existence of in-gap topological second-order corner states is guaranteed by the topological origin of this edge band gap.

4. The second-order topological corner states

It has been shown that inside the topologically nontrivial bulk band gaps there exist topological edge states along the domain walls. Similarly, if the edge band gap mentioned above also possesses nontrivial topological classification, a new type of topological states will emerge at the intersection of two domain walls, namely the second-order topological corner states. The corner modes are spatially very confined near the corners, and they are well isolated from the bulk and edge states in the frequency spectrum.

To illustrate this point, we consider a hexagon-shaped crystal stacked by type A unit cells (colored in blue) coated by a type B cells (red) which features a global C_{6v} symmetry that is compatible with the symmetry of the unit cell, as depicted in Fig. 5(a). These two types of lattices possess different topological invariants χ , that is $\chi = (0, 0)$ for lattice A while $\chi = (-2, 0)$ for lattice B , as we have already stated. Each vertex of the inner hexagon region is the intersection of two 120° -angled neighboring topological interfaces. Note that the 60° -angled interface corresponding to a triangular

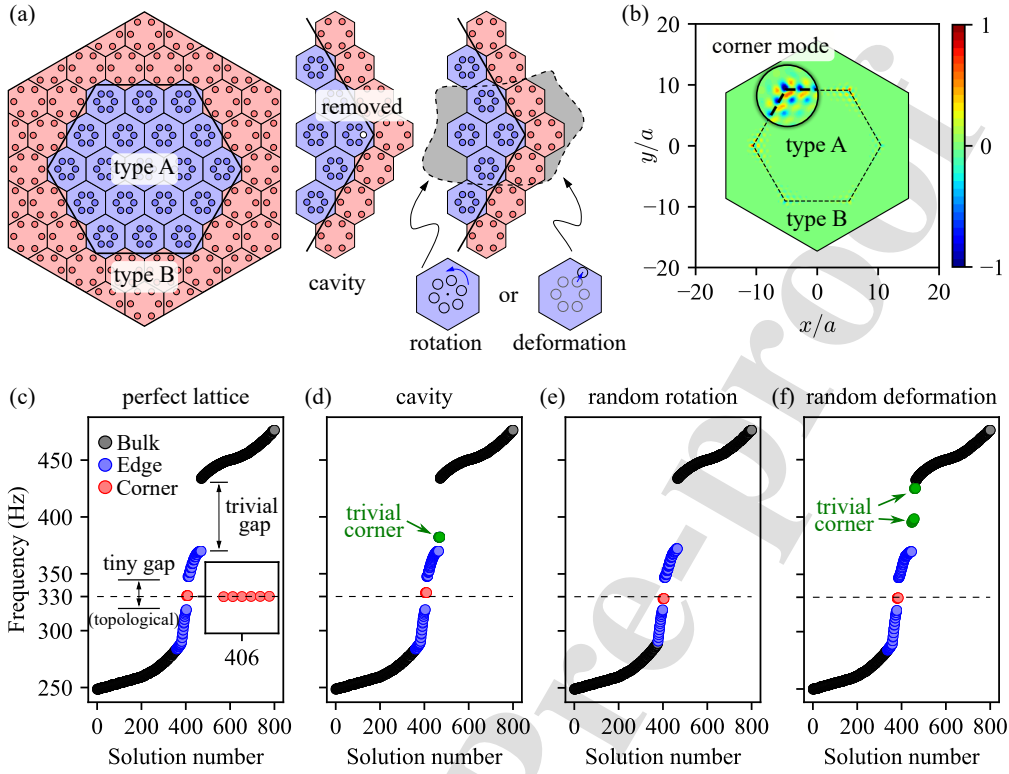


Figure 5: **The second-order topological corner states.** (a) The schematic view of the hexagonal structure and various lattice imperfections. (b) The normalized out-of-plane displacement distribution of the corner state. (c)-(f) The eigenfrequency spectra of the lattice structure under various geometrical perturbations: (c) without any perturbations, (d) with a cavity, or disorders introduced by randomly (e) rotating or (f) deforming several cells near each corner.

shape lattice A is not considered here for two reasons, the first reason is the lattice termination or interfaces should be compatible with the unit cell symmetry [51], and the second reason is that the corner states at obtuse-angled corners are topologically protected while those at acute-angled corners are not [52]. Besides the perfect periodic structure, we also introduced three types of perturbations on the crystal to demonstrate the robustness of the corner states with topological protection, including a cavity by removing one resonator near the corner, or disorders induced by randomly rotating or deforming seven-unit cells close to the corner, schematically shown in the right panels in Fig. 5(a). The calculated eigenfrequency spectra for the perfect and perturbed crystals are shown in Fig. 5(c) – (f), and a typical mode shape corresponding to one of the six corner states highlighted by red dots in Fig. 5(c) for the perfect lattice is plotted in Fig. 5(b). The result in Fig. 5(c) again illustrates the existences of topological edge states (blue dots), and more importantly

the in-gap topological second-order corner states (red dots, around 335 Hz), which are not directly predictable from the edge-projected band diagrams. The spatial localization of the corner states is unambiguously demonstrated by the eigenmode distribution, in which only a small region near the corners has nonzero out-of-plane displacements.

Ensured by their topological origin, the in-gap topological second-order corner states are not only frequency-isolated but also are robust against structure imperfections as long as the lattices on both sides of the interface hold the topological classification. In other words, the corner-localized modes will be preserved, and their corresponding eigenfrequencies won't deviate too much from the original values in the presence of various types of perturbations on the perfect lattice (without closing the bulk gap), such as removing resonators, randomly rotating or deforming several unit cells near the corners. The eigenfrequencies of the perturbed crystals for these three cases are listed in Fig. 5(d) – (f). Comparing them with Fig. 5(c) reflects two important facts: the first one is that the eigenfrequencies of the in-gap topological corner states almost remain unchanged, and the second one is that inside the trivial gap, the trivial corner modes (green dots), however, either appear or disappear under different circumstances. Even in the case of their presence, the trivial corner modes may emerge at different frequencies or even come into multiple groups, completely dependent on the specific perturbed crystal, which makes them much less useful when compared with the robust topological corner modes.

5. Occurrence of topological Fano resonance

We propose a three-component phononic plate structure, as shown in Fig. 6(a), to investigate the Fano resonances induced by the coupling between topological edge states and the second-order corner states. This phononic crystal is composed of 11 layers of type A' lattices ($R/R_0 = 0.9$) on the upper half, and 11 layers of type B lattices ($R/R_0 = 1.3$) on the lower half but with a semi-hexagon region replaced by type A lattices ($R/R_0 = 0.7$). According to our previous discussions, the A'/B interface supports nearly gapless topological edge states (termed as the bright mode), and the A/B interfaces support the gapped edge states and the in-gap second-order corner states (termed as the dark mode). One can anticipate that the bright mode and dark mode will undergo very strong interactions around the resonant frequency, while at other frequencies their couplings are negligible. Moreover, the phase variation of the bright mode is continuous and slow, but the

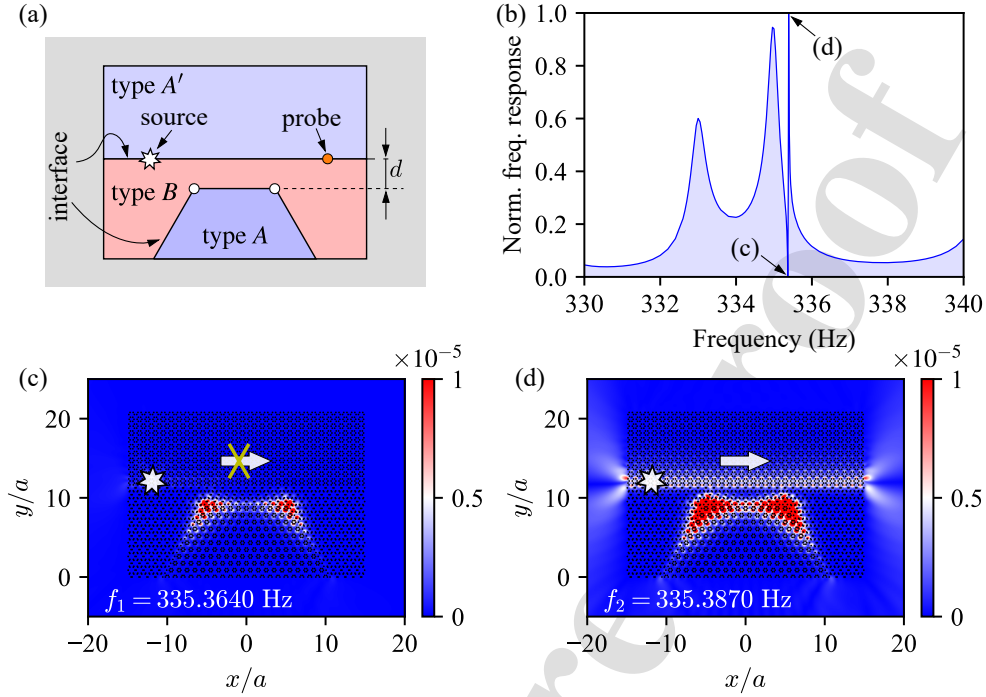


Figure 6: **The occurrence of topological Fano resonance.** (a) schematic view of a sandwiched lattice with $A'/B/A$ configuration that supports the coupling between topological edge states and second-order corner modes. (b) The normalized frequency response of the topological edge state. (c) and (d) the wave fields magnitudes $|w(x, y)|$ at the dip- and peak-frequency, respectively.

dark mode has a phase shift of π near the resonant frequency, leading to a transition from an out-of-phase interference to an in-phase one, or vice versa. This abrupt change finally creates an asymmetric lineshape in the frequency response within a very narrow band, which is a Fano-like resonance with topological origins for both the bright and dark modes.

The FEM-based method in previous sections are suitable for band structure (eigenproblems) calculations, while hereafter we turn to utilize the computationally efficient multiple scattering method (MST) [29] (see Appendix E for details) to simulate the wave field distributions and frequency response of the proposed lattice under a specific source excitation. Note that even the MST based on the Kirchhoff-Love plate theory is valid only for low frequencies and long wavelength limit, the MST simulated results show good correspondence with the FEM calculated bandgaps (see Fig. 4 and Fig. C.11 for comparison). Fig. 6(b) shows the MST simulated frequency response with respect to its maximum. Here the frequency response is defined as the ratio between

the detected displacement signal and the excited source signal. In the calculation, we have set $d = 3d_0$ where $d_0 = \sqrt{3}a/2$ is the height of each unit cell, and the wave field is excited by a unit-magnitude point source. Around the resonant frequency of corner modes (~ 335 Hz), we can clearly see the resultant asymmetric and ultra-sharp Fano line. It reaches the maximum very quickly at $f_2 = 335.3870$ Hz from the minimum at $f_1 = 335.3640$ Hz, and the ratio between the maximum and the minimum is $1/(3.557 \times 10^{-3}) = 281$. The Q-factor for the Fano resonance is given by the ratio between the average frequency and the frequency difference of the peak and dip value [66], based on which we found the Fano resonance here has an ultrahigh value that $Q = f_0/\Delta f = 14582$. The out-of-plane displacement distributions excited by a unit-magnitude point source at f_1 and f_2 are shown in Fig. 6(c) and (d), respectively, which vividly demonstrate the forbidden and pass states due to the destructive and constructive interference between the bright and dark modes. This ultra-sensitive switching phenomenon may provide potential applications in acoustic sensors or switches. Moreover, because both the bright and dark modes, the fundamental ingredients to create the Fano resonance, have the topological protection features, this particular type of Fano resonance may stand out from its conventional counterparts as it is more robust against structural imperfections.

The lattice configurations for other values of d will affect the peak- and dip-value of the Fano resonance, but the resonant frequency, as well as the ultra-sharp and asymmetric features of the response curve will be preserved. The frequency responses of the topological edge states coupled with the corner modes at different values of d are shown in Fig. 7(b)-(e). As a reference, the edge states frequency response without edge-corner couplings are also displayed in Fig. 7(a), which is in fact a zoom-in view of Fig. C.11(d). The main profile of the frequency response in Fig. 7(a), especially the two large broad peaks around 333 and 335 Hz, are maintained even in the presence of the edge-corner couplings. The significant result of the edge-corner coupling is the emergence of the Fano resonance. In addition, by comparing Fig. 7(c)-(e), it can be concluded that larger values of d means weaker coupling strengths, which will decrease the ratio between the peak- and dip- values, making the Fano resonance less observable. Note that around the Fano resonance, the response changes abruptly, thus a very fine frequency sweep are needed, as shown in the insets.

It is also worth noting that for $d = 2d_0$, the edge-corner distance is too close such that the response is affected strongly by the corner modes, and presents a different behavior with other cases. To qualitatively explain this, we simplify the topological lattice system into a 3 degree-

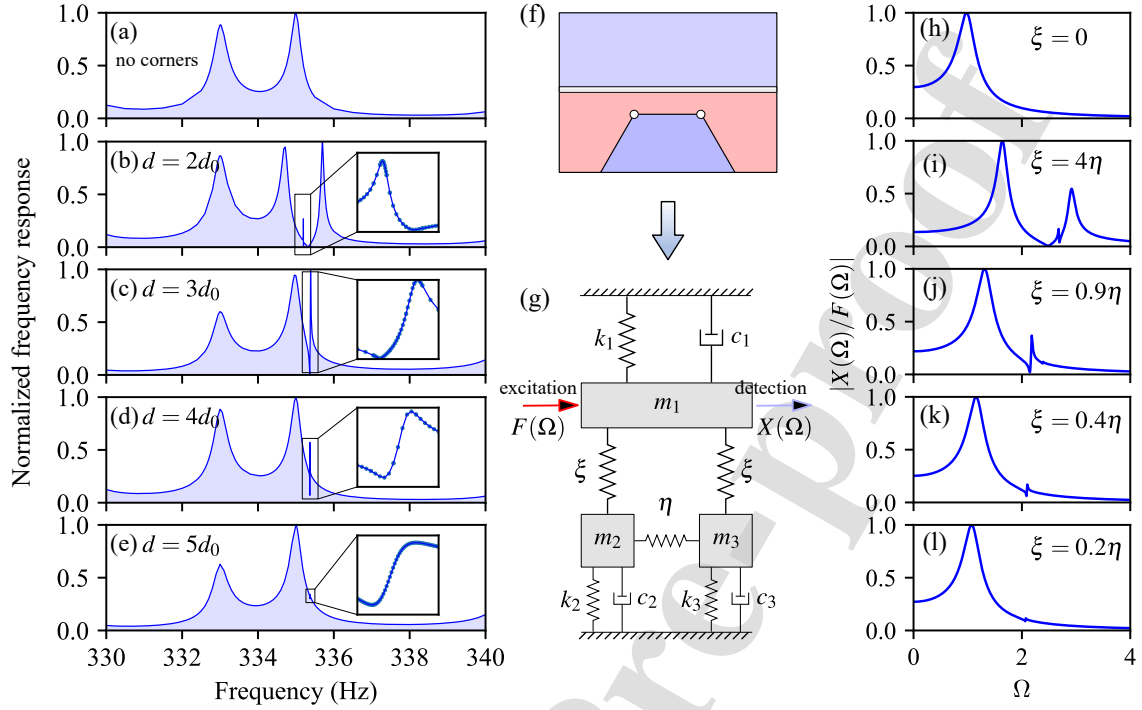


Figure 7: **Fano lineshapes in the MST simulated frequency responses for various edge/corner distances.** (a) The frequency response for the A'/B edge states. (b)-(d) correspond to $d = 2d_0$ to $5d_0$ with d_0 the height of one unit cell. The insets show sufficient fine sweep of the response spectra near the Fano resonant frequency in the numerical calculations. (f) The schematic view of the lattice configuration that supports edge-corner couplings. (g) The simplified discrete 3 degree-of-freedom (DOF) mass-spring system. (h)-(l) The frequency response for the 3-DOF system in (g) for various values of coupling strengths ξ . The dimensionless parameters are $k_1 = 1, m_1 = 1, c_1 = 0.3, k_2 = 4, m_2 = 1, c_2 = 0.01, k_3 = 1.1k_2, m_3 = m_2, c_3 = c_2, \eta = 0.5$, and ξ is the tuning parameter.

of-freedom (DOF) system as shown in Fig. 7(f)-(g). Since the both corners states are isolated modes, thus they can be viewed as a 1-DOF oscillator with very small damping ratio, while the broad band topological edge states span over a broad spectrum, thus an oscillator with a large damping ratio is needed to exhibit a similar behavior (see the particular parameters we chose in Fig. 7). Next, we apply a force $F(\Omega)$ on m_1 and record its displacement response $X(\Omega)$ and obtain the frequency response function $H(\Omega) = X(\Omega)/F(\Omega)$ where Ω is the dimensionless angular frequency. The amplitudes of $H(\Omega)$ for various values of ξ are plotted in Fig. 7(h)-(l). Here ξ denotes the coupling strength between m_1 and $m_{2,3}$, directly mimicking the couplings between the topological edge and corners. If we ignore the first peak in Fig. 7(a)-(e), it can be seen that

our simplified 3-DOF system matches well with the real topological edge/corner coupling lattice by comparing the frequency responses of both systems. Note that the two corner modes are not completely degenerate, thus we have let k_3 slightly deviates from k_2 . Through the calculation on the 3-DOF system, we found that there are in fact always two Fano resonant peaks [see Fig.7(i)], corresponding the two corners. The competition between edge-corner coupling (ξ) and the corner-corner coupling (η) determines which one of the two Fano profiles is dominant. For $\xi = 4\eta$, both Fano profiles are observable, which explains Fig.7(a). As the coupling strength ξ decreases shown in Fig.7(j)-(l), both Fano resonances decrease quickly and only one of them is detectable, which explains Fig.7(c)-(e).

6. Robustness of topological Fano resonance

In this section, we investigate the robustness of the topological Fano resonance when various types of structural imperfections are deliberately introduced into the system. From the discussions in the previous sections, we know that the Fano resonance occurs around the resonant frequency of the dark mode, i.e., the topological second-order corner mode. So, it is natural to consider that the corner mode influences the Fano resonance more significantly, therefore we focus on the variations of the frequency response for the structural imperfections acting on the corners.

As a first example, we consider the rotational perturbations by assigning random rotational angles (schematically illustrated in Fig. 5(a)) independently for each of the seven cells around the corners. For simplification, both corners are set to be under exactly the same perturbation. The random angles are given with an increasing of the angle magnitudes, from $|\theta| < 5^\circ$ to $|\theta| < 10^\circ$.

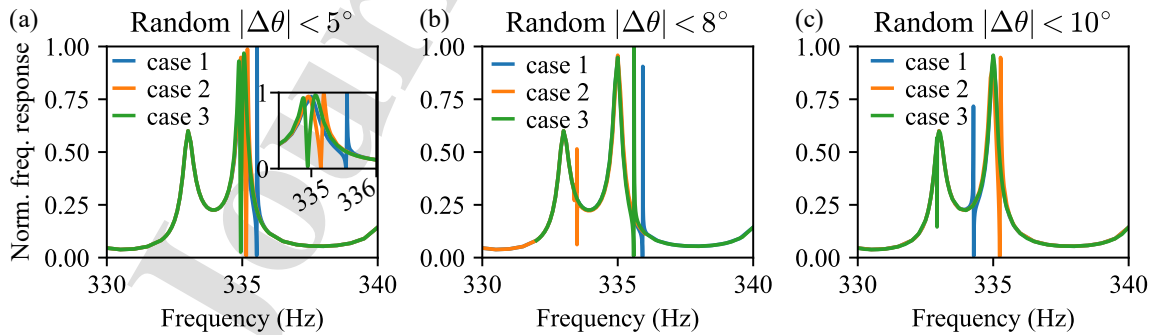


Figure 8: **The robustness of the topological Fano resonance when different random rotational angles are introduced** for (a) $|\Delta\theta| < 5^\circ$, (b) $|\Delta\theta| < 8^\circ$ and (c) $|\Delta\theta| < 10^\circ$ when $d = 3d_0$.

For each perturbative level, we generate 3 different groups of the random angles and repeat the calculation for each of them. From the results listed in Fig. 8, we can conclude that the Fano shape response is always preserved even though the resonant frequency may deviate slightly from the original point. As the magnitudes of the angles increase, the frequency shift of the Fano resonance tends to take a larger value. However, even for the case that $|\theta| < 10^\circ$, we can see the largest relative frequency shift is approximately estimated as $|333 - 335|/335 \approx 0.6\%$, which is very small.

Then we investigate the influences of the deformations by assigning independent random resonator to centroid distances on the same seven cells considered above. Similar to the case of rotational perturbations, here we also consider different magnitudes of the distances in an increasing manner from $|\Delta R/R_0| < 5\%$ to $|\Delta R/R_0| < 10\%$, and for each level we also generate 3 groups of geometrical configurations, upon which the calculation is repeated. The results shown in Fig. 9 are very similar to those shown in Fig. 8 for the rotational cases, from which we can conclude again that the Fano lineshape response is always preserved, and the frequency shift is comparatively small even we impose the maximum value of 10% geometrical perturbations.

Note that if we remove one resonator around the corner as we did in Fig. 5(a), we can expect that the influence on the Fano resonance is also neglectable (not shown) since the eigenfrequency spectrum in Fig. 5(d) reveals that the topological corner modes are very robust. We compare the topological corner states and trivial defects with disorders in Appendix D, which indicates that the frequency of the topological corner states still remains in the gap of edge states and are only perturbed slightly, while the trivial point defect with disorders will suffer a huge shift across the whole bandgap of the bulk states. This unambiguously reflects the robustness of the topological

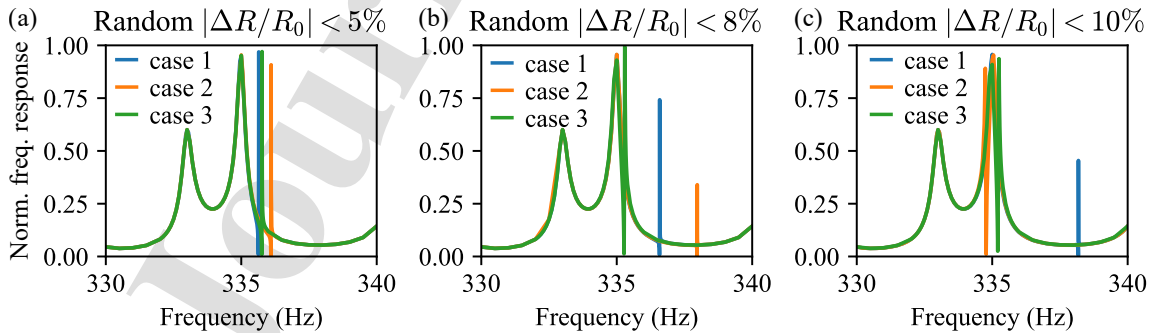


Figure 9: **The robustness of the topological Fano resonance when different random resonator-centroid distances are introduced** for (a) $|\Delta R/R_0| < 5\%$, (b) $|\Delta R/R_0| < 8\%$ and (c) $|\Delta R/R_0| < 10\%$ when $d = 3d_0$.

corner modes and topological Fano resonance.

7. Discussions and Conclusions

In conclusion, we have investigated the topological Fano resonance induced by the interference between the first-order topological edge states and the second-order topological corner modes by taking an elastic phononic crystal plate as an example object. The breathing honeycomb lattice under consideration in this work is capable of hosting simultaneous topological edge states and corner states, which can be achieved simply by tuning the geometrical parameters. When both topological states are integrated into the same platform, they can have the possibility to couple with each other. Hence, the constructive and destructive interferences between them result in the ultra-sharp and asymmetric Fano resonance. Because both of the bright and dark modes are topologically protected, the resultant Fano resonance features a unique advantage of robustness against various kinds of geometrical imperfections, which is also quantitatively confirmed by our numerical calculations.

We also demonstrated that the coupling strength between the topological edge and corner modes has a significant influence on the Fano-like spectrum. As the distance between the edge and corners increasing, the coupling strength decreases gradually, weakening the resultant topological Fano resonance. By qualitatively simplify the elastic continuum structure into a 3-DOF system, we found that if the two corner modes are not rigorously degenerate, there are in fact two Fano resonant profiles. The relative magnitudes of these two Fanos depends on the competition between the edge/corner and corner/corner couplings. In our case, only for $d = 2d_0$ could we observe two Fano resonance, while once $d \geq d_0$, one of them almost disappears and becomes not detectable. Furthermore, we found that if two corners are placed with unequal distances from the topological edge, two nested ultra-sharp peak-dip pairs will also emerge.

It is worth noting that the lossless phononic plate attached with mass-spring resonators proposed here is a prototype design. For practical considerations, We discussed in [Appendix G](#) the effects of dissipation and concluded that the increasing of the loss coefficient will gradually flatten the ultra-sharp Fano line-shape and the large peak-dip discrepancy. If the loss coefficient is large enough, the asymmetric Fano line will be eased out and the Q factor decreases quickly. For the experimental realization of the proposed robust Fano resonance, we suggest a more physically accessible way to model the mass-spring resonators by using elastic pillars in the future experimental works, such as

on-chip micromechanical phononic plates with pillars etched on silicon chips [33, 56], or similar arrangements on the macroscale phononic crystals by using 3D printing [67] or other techniques [57, 68]. Our findings may find applications in highly sensitive and accurate filters, sensors, and switches.

During the submission of this paper, we became aware of Ref. [69] which also utilized the SO-TIs to realize the robust dark modes to construct a topological Fano resonance in photonic crystals. We would like to note that Ref. [69] adopted both armchair and zigzag topological interfaces to realize gapless topological edge states and in-gap corner modes with common frequencies to further guarantee the Fano interaction, while in our work it is simply realized by independently tuning the geometrical configurations of unit cells in different regions of the phononic crystal, and only one type of topological interface is needed.

Acknowledgments

Y. W. acknowledges the support from China Postdoctoral Science Foundation (No. 2020M672615). R. Z. acknowledges the financial support from the National Natural Science Foundation of China (Grant No. 12102103).

Appendix A. Symmetry reconstruction of degenerate eigenmodes

The Bloch modes usually exhibit certain symmetries at high-symmetric point in the reciprocal space. But for degenerate modes, these symmetries might be hidden because of mode hybridization, which is very common in numerical simulations. In this section we demonstrate how to recover the symmetry of the modes from the hybridized ones, which is very useful for topological index analysis and effective Hamiltonian deduction.

As shown in Fig. A.10, $\psi_i (i = 1, 2, 3, 4)$ are four degenerate eigenmodes at the double Dirac cone, which are clearly hybridized due to the indetermination resulting from numerical calculation in FEM analysis. Our strategy is as follows: first, to find some linear combination of ψ_i such that the new modes φ_i can be grouped into two categories (φ_1, φ_2) and (φ_3, φ_4) , depending on their corresponding eigenvalues of \hat{r}_2 operation (rotating 180° about the origin), as depicted in the second row of Fig. A.10. Similarly, the second step is to find some linear combination of (φ_1, φ_2) , such that the new modes (ϕ_1, ϕ_2) can be distinguished by their parities, and the same for (ϕ_3, ϕ_4) , as shown in

the last row of Fig. A.10. The key of these two steps is to find the mentioned linear combinations. Below we demonstrate how to fulfill it by taking the first step as an example.

Suppose the four modes ψ_i ($i = 1, 2, 3, 4$) satisfy the following eigenvalue problem,

$$H\psi_i = \lambda\psi_i \quad (\text{A.1})$$

And the rotation operator \hat{r}_2 commutes with H , which means

$$\hat{r}_2 H = H \hat{r}_2 \quad (\text{A.2})$$

Now let H act on $\hat{r}_2\psi_i$, we have

$$H\hat{r}_2\psi_i = \hat{r}_2 H\psi_i = \hat{r}_2(\lambda\psi_i) = \lambda(\hat{r}_2\psi_i) \quad (\text{A.3})$$

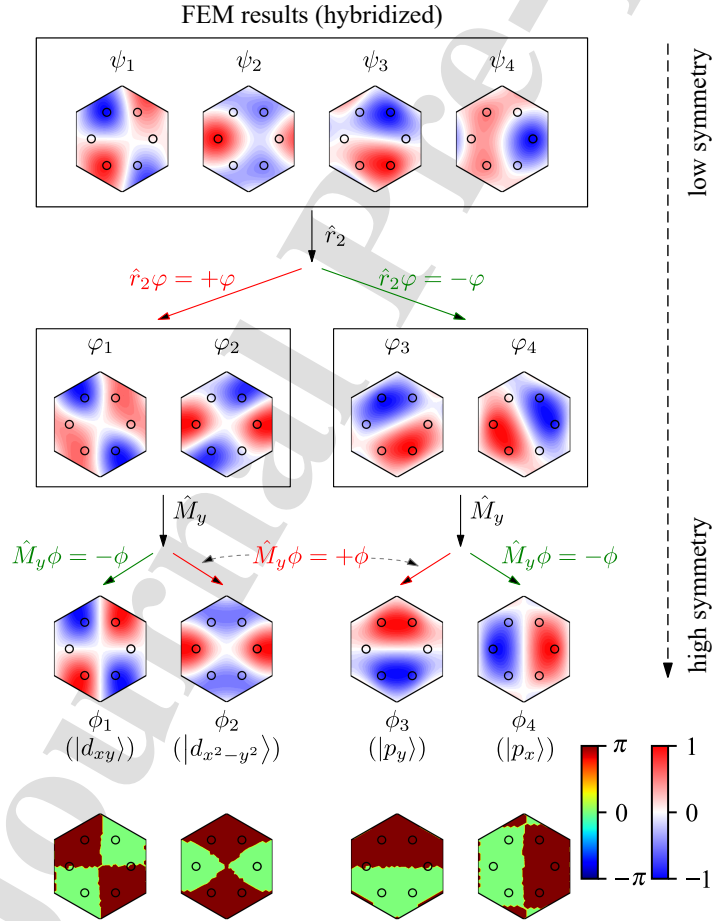


Figure A.10: The reconstruction of the symmetric eigenmodes from the hybridized modes. The phases of these modes are also shown to illustrate their rational eigenvalues.

which unambiguously reveals that $\hat{r}_2\psi_i$ is also an eigenvector of H , corresponding to the same eigenvalue λ . Therefore, $\hat{r}_2\psi_i$ must lie in the subspace spanned by $\psi_i (i = 1, 2, 3, 4)$,

$$\hat{r}_2\psi_i = \sum_{j=1}^4 S_{ij}\psi_j \quad (\text{A.4})$$

in which S_{ij} represent some expansion coefficients that can be identified as

$$S_{ij} = \langle \hat{r}_2\psi_i, \psi_j \rangle \quad (\text{A.5})$$

Once the 4×4 matrix S is obtained, we consider the following eigenvalue problem

$$S^T v = \eta v \quad (\text{A.6})$$

in which η and v are the eigenvalue and eigenvector of S^T . Now let v be the coordinate of some vector in $\text{span}\{\psi_i\}$, denoted as φ , which means

$$\varphi = \sum_{i=1}^4 v_i \psi_i \quad (\text{A.7})$$

Therefore, $\hat{r}_2\varphi$ can be evaluated as follows,

$$\hat{r}_2\varphi = \sum_{i=1}^4 v_i \hat{r}_2\psi_i = \sum_{i=1}^4 v_i \sum_{j=1}^4 S_{ij}\psi_j = \sum_{j=1}^4 \psi_j \sum_{i=1}^4 v_i S_{ij} = \sum_{j=1}^4 \psi_j \eta v_j = \eta \varphi \quad (\text{A.8})$$

We find that φ is an eigenvector of \hat{r}_2 , with the corresponding eigenvalue being η . This reveals that φ defined in Eq. (A.7) is symmetric under the operation \hat{r}_2 .

The aforementioned procedure indeed helps us to transform ψ_i to φ_i , as shown in the second row of Fig. A.10. By applying similar method, we can finally obtain the four modes listed in the third row of Fig. A.10, with well recovered symmetries.

Appendix B. The effective Hamiltonian by $k \cdot p$ method

In this section we give the explicit form of the reduced effective Hamiltonian of the continuum elastic system by using the $k \cdot p$ perturbation method. We start from a group of eigenfrequencies ω_{nk_0} and their corresponding eigenmodes w_{nk_0} at k_0 point, which can be numerically obtained by the method illustrated in Sec. 2 and Appendix A. With these eigen-solutions at hand, the eigenmodes at $k_0 + \Delta k$ are supposed to be the linear superposition of w_{nk_0} , and are inserted back into the

equation of motion, which gives rise up to a small matrix eigenvalue problem, i.e., the effective Hamiltonian \mathcal{H} . By taking the symmetry properties of the eigenmodes w_{nk_0} into consideration, it is demonstrated that the explicit form of the effective Hamiltonian can be obtained without explicitly solving the eigenvalue problem. Furthermore, by analytically solving the eigenvalue, the results show good agreements with that from the FEM simulations for small $|\Delta\mathbf{k}|$, as shown in Fig 3.

We consider the bands in the vicinity of Γ point ($\mathbf{k}_0 = \mathbf{0}$), by first expanding the cell-periodic counterpart of the Bloch wave at $\mathbf{k} = \Delta\mathbf{k}$ in terms of those at Γ ,

$$\hat{w}_{nk}(\mathbf{r}) = \sum_l A_{nl}(\mathbf{k}) \hat{w}_{l\Gamma}(\mathbf{r}) \quad (\text{B.1})$$

where A is the \mathbf{k} -dependent expansion coefficient. Inserting this expression back into Eq. (5) we have

$$w_{nk}(\mathbf{r}) = \exp(i\mathbf{k} \cdot \mathbf{r}) \sum_l A_{nl}(\mathbf{k}) w_{l\Gamma}(\mathbf{r}) \quad (\text{B.2})$$

For simplification and compactness, from hereafter, we adopt the biharmonic equation for flexural wave in which the field $w_{nk}(\mathbf{r})$ is governed as

$$D\nabla^2[\nabla^2 w_{nk}(\mathbf{r})] - \rho h \omega^2 w_{nk}(\mathbf{r}) = f_z(\mathbf{r}) \quad (\text{B.3})$$

Similar to our previous work [39], by substituting Eq. (B.2) into Eq. (B.3), we have

$$\sum_l A_{nl}(\mathbf{k}) \left[4D\mathbf{k} \cdot i\nabla\nabla^2 - \rho' h (\omega_{nk}^2 - \omega_{n\Gamma}^2) \right] w_{l\Gamma}(\mathbf{r}) = 0 \quad (\text{B.4})$$

in which the higher order of $|\mathbf{k}|$ has been neglected, and the effective mass density ρ' is expressed as

$$\rho' = \rho + \frac{1}{h} \sum_{j=1}^6 m \delta(\mathbf{r} - \mathbf{R}_j) \quad (\text{B.5})$$

in which m and \mathbf{R}_j are the mass and location of the attached resonator, and $\delta(\mathbf{r})$ is the Dirac-delta function. Considering the orthogonality of the Bloch functions,

$$\int_{\text{cell}} \rho' w_{n\Gamma}^*(\mathbf{r}) w_{l\Gamma}(\mathbf{r}) d\mathbf{r} = \delta_{n,l}, \quad (\text{B.6})$$

we arrive at the final eigenvalue problem

$$\sum_l \left[\mathbf{k} \cdot \mathbf{p}_{nl} - (\omega_{nk}^2 - \omega_{n\Gamma}^2) \delta_{n,l} \right] A_{nl} = 0 \quad (\text{B.7})$$

where

$$\mathbf{p}_{nl} = 4D \int_{\text{cell}} w_{n\Gamma}^* \cdot i\nabla(\nabla^2 w_{l\Gamma}) d\mathbf{r} \quad (\text{B.8})$$

As we are interested in the dispersion around the double Dirac cone, and the other bands are far away from the Dirac frequency (Fig. 3), the infinite summation in Eqs. (B.4) and (B.7) can be truncated and only the fourfold degenerate modes are conserved. Therefore, \mathbf{p} is reduced into a 4×4 matrix in which each entry itself is a two-dimensional vector. The reduced Hamiltonian is given by

$$\mathcal{H}_{ij} = \mathbf{k} \cdot \mathbf{p}_{ij} \quad (\text{B.9})$$

Now let us take the symmetry of the eigenmodes into consideration to simplify the above expression. As demonstrated in Fig. 3, the p and d modes have different mirror symmetries along two coordinate axes. These four modes are arranged in the order of $p_x, p_y, d_{x^2-y^2}$ and d_{xy} . Therefore, the calculation of \mathbf{p}_{11} require us to calculate p_x^* and $i\nabla(\nabla^2 p_x)$. To be brief, the parity of all the terms that are involved in the calculation of \mathbf{p}_{11} is listed in Table B.1, in which the sign + (or -) represent the certain term is even (or odd) with respect to the corresponding axis. For example, the signs of the first column in Table B.1 indicate that p_x is odd and even with respect to the x and y axis, respectively. The rest entries can be understood in the same way.

Table B.1: The parity of each term needed in the calculation of \mathbf{p}_{11}

	p_x	$i\partial_x(\nabla^2 p_x)$	$i\partial_y(\nabla^2 p_x)$	$p_x^* \cdot i\partial_x(\nabla^2 p_x)$	$p_x^* \cdot i\partial_y(\nabla^2 p_x)$
x	-	+	-	-	+
y	+	+	-	+	-

According to the last two columns of Table B.1, one can conclude that

$$\int_{\text{cell}} p_x^* \cdot i\partial_x(\nabla^2 p_x) d\mathbf{r} = 0 \quad (\text{B.10a})$$

$$\int_{\text{cell}} p_x^* \cdot i\partial_y(\nabla^2 p_x) d\mathbf{r} = 0 \quad (\text{B.10b})$$

Hence, $\mathbf{p}_{11} = (0, 0)$.

After analyzing all the term of p_{ij} in the similar way, the matrix form of \mathbf{p} is collected as follows

$$\mathbf{p}_{4 \times 4} = \begin{bmatrix} (0,0) & (0,0) & (B^*,0) & (0,B^*) \\ (0,0) & (0,0) & (0,B) & (B^*,0) \\ (B,0) & (0,B^*) & (0,0) & (0,0) \\ (0,B) & (B,0) & (0,0) & (0,0) \end{bmatrix} \quad (\text{B.11})$$

in which B is a pure imaginary number which need to be further numerically calculated. Substituting Eq. (B.11) back into Eq. (B.7), we obtain the following eigenvalue problem,

$$\begin{bmatrix} 0 & 0 & B^*k_x & B^*k_y \\ 0 & 0 & Bk_y & B^*k_x \\ Bk_x & B^*k_y & 0 & 0 \\ Bk_y & Bk_x & 0 & 0 \end{bmatrix} A = [\omega^2 - \text{diag}(\omega_p^2, \omega_p^2, \omega_d^2, \omega_d^2)] A \quad (\text{B.12})$$

If we denote $p_{\pm} = (p_x \pm ip_y)/\sqrt{2}$, $d_{\pm} = (d_{x^2-y^2} \pm id_{xy})/\sqrt{2}$, $\omega_0^2 = (\omega_p^2 + \omega_d^2)/2$, and $\Delta = (\omega_d^2 - \omega_p^2)/2$, we arrive at the final eigenvalue problem

$$\mathcal{H}\Phi = \lambda\Phi \quad (\text{B.13})$$

in which the eigenvalue is $\lambda = \omega^2 - \omega_0^2$, with the corresponding eigenvector Φ to be the linear superposition of the expanding coefficients A according to the above base-transformation, and the effective Hamiltonian is given by

$$\mathcal{H} = \begin{bmatrix} -\Delta - \alpha k^2 & B^*k_- & & \\ Bk_+ & \Delta + \alpha k^2 & & \\ & & -\Delta - \alpha k^2 & B^*k_+ \\ & & Bk_- & \Delta + \alpha k^2 \end{bmatrix} \quad (\text{B.14})$$

where $k = |\mathbf{k}|$, $k_{\pm} = k_x \pm ik_y$, and $\alpha = |B|^2/2\Delta$. The eigenvalues of \mathcal{H} are analytically obtained as

$$\omega^2 - \omega_0^2 = \pm \sqrt{(\Delta + \alpha k^2)^2 + |B|^2 k^2} \quad (\text{B.15})$$

which can well describe the real behavior of the band structures in the vicinity of Γ point, as shown in Fig. 3(a), (c) and (d).

Appendix C. The frequency responses for topological edge states

To provide more insights on the topological edge states and the aforementioned tiny gap, we present the frequency response spectrum for the phononic crystal constructed from topologically distinct lattices in Fig. C.11. As schematically illustrated in Fig. C.11(a), the upper half of the presented phononic crystal, being type A (or A') lattice, consists of more than 20 unit cells along the x direction and 8 layers along the y axis, while the lower half made of type B lattice consists of the exact same number of cells, forming a topological interface near the horizontal line $y = 0$. A time-harmonic point source (marked by a star) is placed at the lattice center to excite the flexural waves, and the multiple scattering method calculated out-of-plane displacement near the right outlet is recorded and plotted in Fig. C.11(d) and (e) for A'/B and A/B interfaces, respectively. From Fig. C.11(d) we can clearly see that in the case for A'/B interface, the responses are relatively large in the bulk band gap, meaning the emergence of topological edge states. Fig. C.11(b) shows a typical example of the out-of-plane displacement fields of the exited topological edge states at 335 Hz,

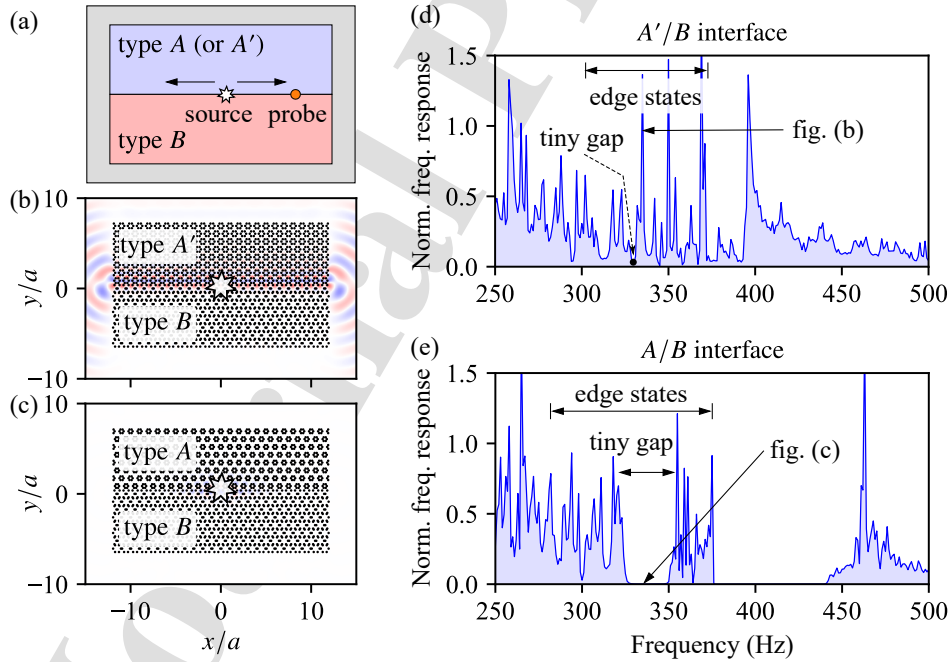


Figure C.11: **The frequency responses for topological edge states of A'/B and A/B interfaces.** (a) The illustration of the lattice configuration. (b) and (c) The wave field distributions for A'/B and A/B lattices at a common frequency marked by black arrows in (d) and (e). (d) and (e) The calculated frequency responses for A'/B and A/B interfaces, respectively.

which is clearly localized near the domain wall. Note that a very tiny gap around 330 Hz can be carefully detected inside the range of the edge states, as predicted by the band structure in Fig 4(b). This tiny gap will become more visible if we enlarge the discrepancy between the two types of lattices, as shown in Fig. C.11(e). In this case, the above excitation frequency lies into the band gap and therefore the corresponding excited wave field shown in Fig. C.11(c) is forbidden to travel along the domain wall.

Appendix D. Comparison between the topological corner and trivial cavity modes

In this section we calculated the eigenfrequency spectrums for the topological corner modes and the trivial cavity modes with/without introducing geometrical defects. As shown in Fig. D.12 (a),

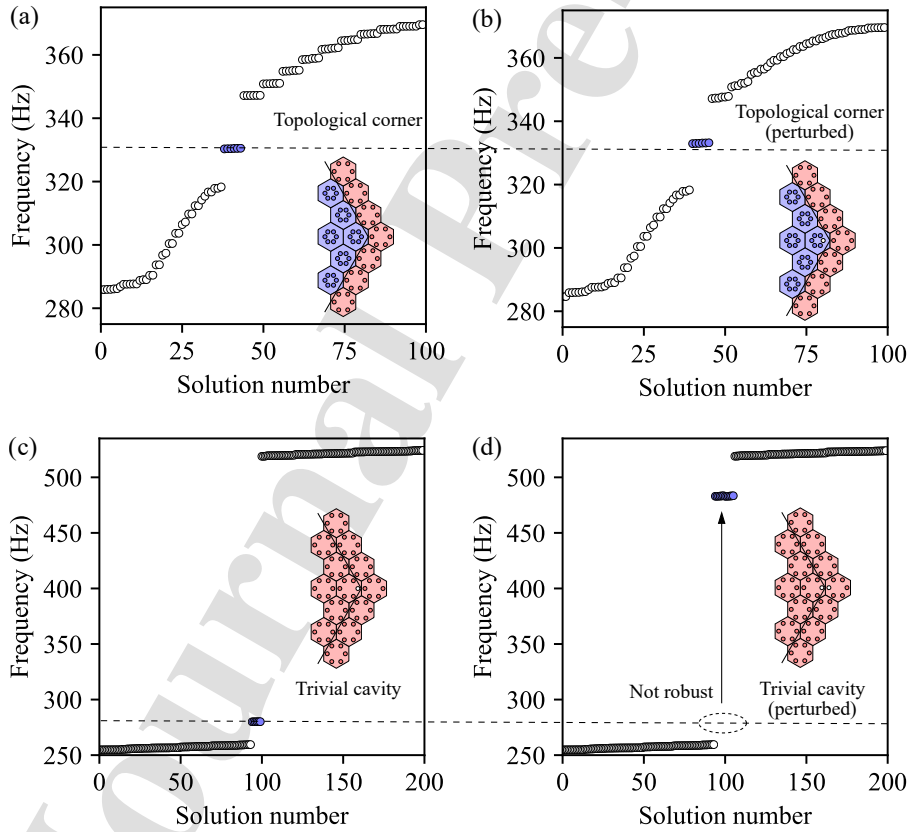


Figure D.12: **Comparison between the robust topological corner modes and the trivial cavity modes.** The eigenfrequency spectrum of the topological corner states (a) with and (b) without perturbations, and the eigenfrequency spectrum of the trivial cavity modes (c) with and (d) without perturbations. The corner modes are highlighted by blue dots. The insets in each figure show a zoom-in view of the corner/cavity of the corresponding structure configurations.

the topological corner is constructed in the same way as shown in Fig. 5(a), and the perturbation on topological corner is realized by removing one resonator near the corner [white dots in the inset of Fig. D.12 (b)]. While the trivial cavity is created by removing one resonator in a single phase lattice ($R/R_0 = 1.3$) as shown in the inset of Fig. D.12 (c), and the perturbation is achieved by removing an additional resonator marked by white dots shown in the inset of Fig. D.12 (d).

It can be seen from Fig. D.12 (a) and (b) that a defect on the topological corner only slightly perturb the frequency of the topological corner states, changing from 330 Hz to 333 Hz (blue dots). While for the trivial cavity, it is evident from Fig. D.12 (c) and (d) that a defect will strongly affect the trivial corner states such that the frequency change from 280 Hz to 483 Hz (blue dots). Therefore, it can be concluded that the topological corner modes are more robust than the trivial cavity modes.

Appendix E. The multiple scattering method for flexural wave in thin plates

In this section we briefly introduce the MST method following Ref.[29] for the total wave field simulations under arbitrary incident wave fields, which is used in this paper for the calculation of wave field distributions and the spectrum response curve. We can rewrite Eq. (B.3) as

$$\nabla^4 w(\mathbf{r}) - \kappa^4 w(\mathbf{r}) = \sum_{\alpha} t_{\alpha} w(\mathbf{R}_{\alpha}) \delta(\mathbf{r} - \mathbf{R}_{\alpha}), \quad (\text{E.1})$$

where $\kappa = (\rho h \omega^2 / D)^{1/4}$ is the wave number in the homogeneous plate, α is a label of the resonators, and t_{α} measures the resonant strength, which is given by

$$t_{\alpha} = \frac{m_{\alpha} \omega^2}{D} \quad (\text{E.2})$$

For truncated finite clusters of resonators, the total wave field distribution under an external incident wave can be semi-analytically solved using MST method: each resonator acts like a point source and radiates a cylindrical wave. The total field is thus the superposition of all the scattered fields and external incident field,

$$w(\mathbf{r}) = w_{\text{inc}}(\mathbf{r}) + \sum_{\alpha} t_{\alpha} w(\mathbf{R}_{\alpha}) G(\mathbf{r}; \mathbf{R}_{\alpha}), \quad (\text{E.3})$$

where $w_{\text{inc}}(\mathbf{r})$ is the incident field which is known beforehand, and $G(\mathbf{r}; \mathbf{R}_{\alpha}) = i/(8\kappa^2)[H_0^{(1)}(\kappa|\mathbf{r} - \mathbf{R}_{\alpha}|) + 2i/\pi K_0(\kappa|\mathbf{r} - \mathbf{R}_{\alpha}|)]$ is the Green's function which satisfies $\nabla^4 w(\mathbf{r}) - \kappa^4 w(\mathbf{r}) = \delta(\mathbf{r} - \mathbf{R}_{\alpha})$ [29].

Considering the total field at an arbitrary resonator's position $\mathbf{r} = \mathbf{R}_\beta$, from Eq.(E.3) we have the linear system

$$\sum_{\alpha} [\delta_{\alpha,\beta} - t_{\alpha} G(\mathbf{R}_\beta; \mathbf{R}_\alpha)] w(\mathbf{R}_\alpha) = w_{\text{inc}}(\mathbf{R}_\beta), \quad (\text{E.4})$$

from which we can derive the displacement of each resonator. The total field can then be constructed by using Eq.(E.3). This semi-analytical method by using Green's function constitutes an efficient approach for the calculations of the total wave field response under any given incident wave.

Appendix F. Double asymmetric Fano profiles by two different waveguide-corner coupling strengths

In this section we consider the case when the distances between the edge and the two corners are different, in which the frequency spectrum exhibits a double Fano-like ultrasharp profiles. Note that we have demonstrated the influence of different values of d on the Fano-line profile in Fig. 7. Since the Fano profile is almost not noticeable for $d \geq 5d_0$, here we study the effects of different coupling strengths by considering $d_1 = 3d_0$ and $d_2 = 4d_0$ as shown in Fig. F.13(a). Again, a source and a detector are placed near the left and right port of the A'/B domain wall. The MST calculated frequency response (solid red curve) is plotted in Fig. F.13(b) and the result for $d_1 = 3d_0$ and $d_2 = 3d_0$ (dashed blue curve) is also shown for comparison. It can be clearly seen from Fig. F.13(b) that the ultrasharp asymmetric Fano-line profile still exists, the magnitude of which reaches from almost zero to nearly unit very quickly, except the frequency has been slightly shift compared with the case for two identical coupling strengths. The different point is that besides this giant asymmetric Fano-line (denoted as Fano 1), we can observe another asymmetric spectrum curve resides into the frequency interval of Fano 1, which we denote as Fano 2 [see the inset of Fig. F.13(b)]. This phenomenon behaves like a hierarchy of Fano resonances. The Fano 2 also experiences an abrupt change in response magnitudes versus frequency, though the change of magnitudes is very small. This can be ascribed to the weaker coupling strength for $d_2 = 4d_0$. We have further increased the value of d_2 such that $d_1 = 3d_0$ and $d_2 = 5d_0$, in which case we found the Fano 2 disappears and can not be detected even we adopted a finer frequency sweeping step (thus the result is not shown here).

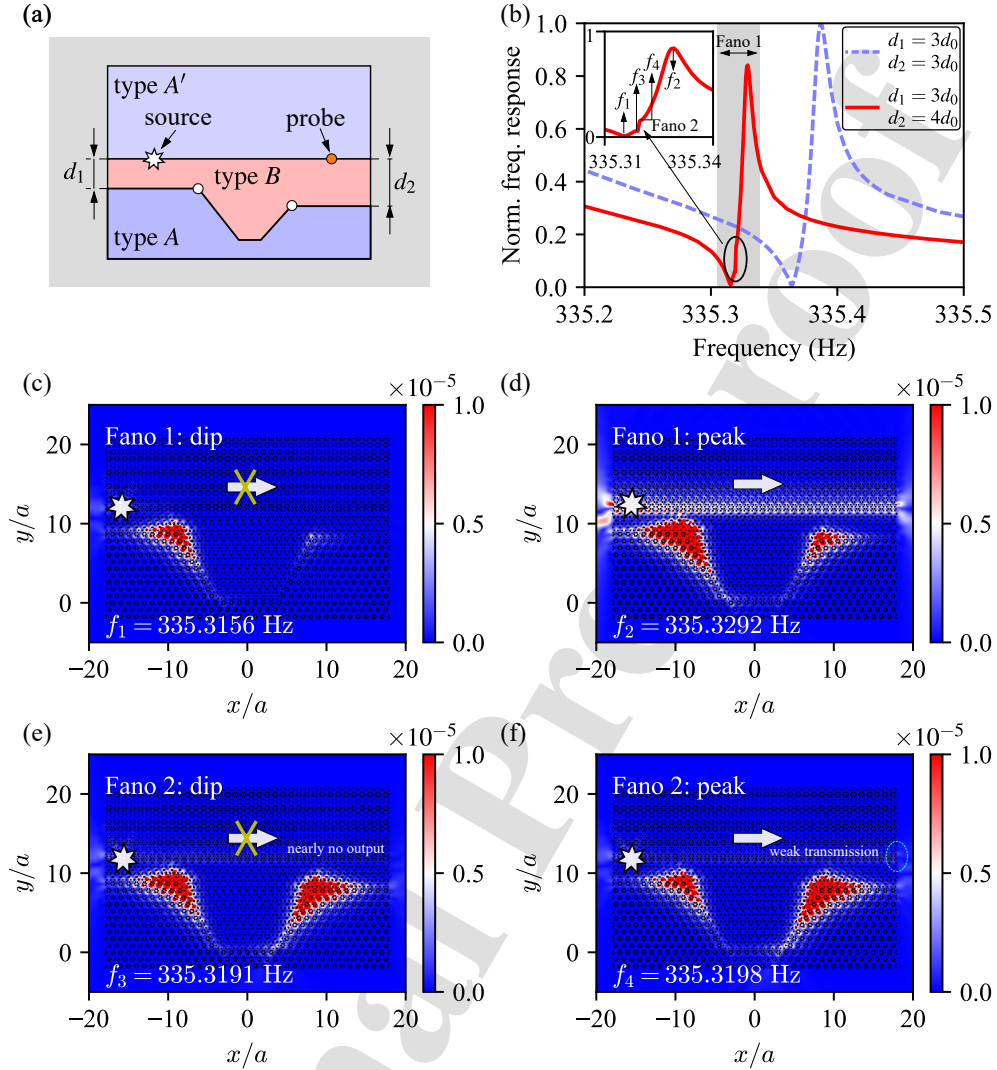


Figure F.13: **Double asymmetric Fano profiles by two different waveguide-corner coupling strengths.** (a) schematic view of a sandwiched lattice with A'/B/A configuration that supports two different waveguide-corner coupling strengths. (b) The normalized frequency response of the topological waveguide. (c) and (d) the wave fields magnitudes $|w(x,y)|$ at the dip- and peak-frequency for the giant Fano-line profile (Fano 1), respectively. (e) and (f) the wave fields magnitudes $|w(x,y)|$ at the dip- and peak-frequency for the tiny Fano-line profile (Fano 2), respectively. Note that the frequency sweeping step is fine enough in the calculation to ensure the ultrasharp Fano-line profiles are obtained correctly.

We have also shown the wave field distributions for the dip and peak frequencies for both Fano 1 and Fano 2. At the dip frequency of Fano 1, the detected signal at the right port is almost zero, which is further confirmed by Fig. F.13(c), in which the topological edge state is not excited while

only one corner mode has a large magnitude. As for the peak of Fano 2, we can see topological edge state and both corner modes are excited. In the case for Fano 2, both at the dip and peak frequencies the two corner modes are excited, and the edge mode discrepancy between the dip and peak is not as evident as that for Fano 1.

Appendix G. The loss effects on the Fano resonance

In practical situations, the loss effects of the dissipation should be taken into consideration. We consider again the three-component phononic crystal illustrated in Fig. 6(a). The geometrical parameters remain the same as the lossless case, and the only difference is that we introduced a complex-valued Young's modulus such that $E' = E_0(1 + i\eta)$ where E_0 is the modulus without loss and the parameter η is a coefficient to account for the loss effects. A harmonic point source is applied on the topological waveguide near the left port, and the simulated out-of-plane displacement on the waveguide near the right port is recorded. The magnitude of the frequency response, i.e., the ratio between the detected signal and the source signal, is plotted below for various choices of η . Note that the lossless case [Fig. 6(b)] is also shown by dashed blue line for reference. We can clearly see that as the loss coefficient η increases, the ultrasharp Fano line-shape and the large peak-dip are flattened gradually. If the loss coefficient is large enough, the asymmetric Fano line will be eased out and the Q factor decreases quickly.

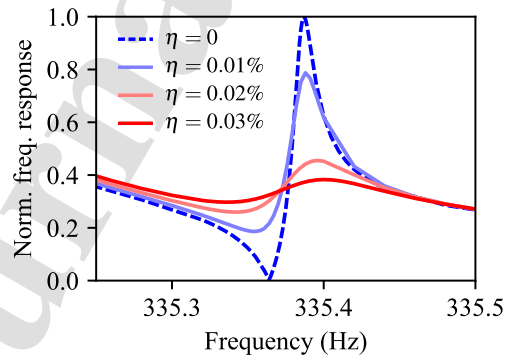


Figure G.14: **The influence of the loss effects on the Fano line-shape spectrum response.** The loss is introduced by using a complex-valued Young's modulus $E' = E_0(1 + i\eta)$ for the plate material. The calculated displacement responses for all cases are normalized with respect to the same factor, i.e., the maximum of the lossless response spectrum.

References

- [1] U. Fano, Effects of configuration interaction on intensities and phase shifts, *Physical Review* 124 (1961) 1866–1878.
- [2] S. Fan, J. D. Joannopoulos, Analysis of guided resonances in photonic crystal slabs, *Physical Review B* 65 (2002) 235112.
- [3] M. V. Rybin, A. B. Khanikaev, M. Inoue, K. B. Samusev, M. J. Steel, G. Yushin, M. F. Limonov, Fano resonance between Mie and Bragg scattering in photonic crystals, *Physical Review Letters* 103 (2009) 023901.
- [4] B. Luk'yanchuk, N. I. Zheludev, S. A. Maier, N. J. Halas, P. Nordlander, H. Giessen, C. T. Chong, The Fano resonance in plasmonic nanostructures and metamaterials, *Nature Materials* 9 (2010) 707–715.
- [5] A. B. Khanikaev, C. Wu, G. Shvets, Fano-resonant metamaterials and their applications, *Nanophotonics* 2 (2013) 247–264.
- [6] C. Goffaux, J. Sánchez-Dehesa, A. L. Yeyati, P. Lambin, A. Khelif, J. O. Vasseur, B. Djafari-Rouhani, Evidence of Fano-like interference phenomena in locally resonant materials, *Physical Review Letters* 88 (2002) 225502.
- [7] Y. S. Joe, A. M. Satanin, C. S. Kim, Classical analogy of Fano resonances, *Physica Scripta* 74 (2006) 259–266.
- [8] A. Fellay, F. Gagel, K. Maschke, A. Virlouvet, A. Khater, Scattering of vibrational waves in perturbed quasi-one-dimensional multichannel waveguides, *Physical Review B* 55 (1997) 1707–1717.
- [9] C. Goffaux, J. Sánchez-Dehesa, P. Lambin, Comparison of the sound attenuation efficiency of locally resonant materials and elastic band-gap structures, *Physical Review B* 70 (2004) 184302.

- [10] Y. A. Kosevich, C. Goffaux, J. Sánchez-Dehesa, Fano-like resonance phenomena by flexural shell modes in sound transmission through two-dimensional periodic arrays of thin-walled hollow cylinders, *Physical Review B* 74 (2006) 012301.
- [11] F. Liu, F. Cai, Y. Ding, Z. Liu, Tunable transmission spectra of acoustic waves through double phononic crystal slabs, *Applied Physics Letters* 92 (2008) 103504.
- [12] Y. Pennec, B. D. Rouhani, H. Larabi, A. Akjouj, G. Lévêque, Perpendicular transmission of acoustic waves between two substrates connected by sub-wavelength pillars, *New Journal of Physics* 14 (2012) 073039.
- [13] S. Amoudache, R. Moiseyenko, Y. Pennec, B. D. Rouhani, A. Khater, R. Lucklum, R. Tigrine, Optical and acoustic sensing using Fano-like resonances in dual phononic and photonic crystal plate, *Journal of Applied Physics* 119 (2016) 114502.
- [14] Y. Jin, E. H. E. Boudouti, Y. Pennec, B. Djafari-Rouhani, Tunable Fano resonances of Lamb modes in a pillared metasurface, *Journal of Physics D: Applied Physics* 50 (2017) 425304.
- [15] F. Zangeneh-Nejad, R. Fleury, Topological Fano Resonances, *Physical Review Letters* 122 (2019) 014301.
- [16] M. Z. Hasan, C. L. Kane, *Colloquium* : Topological insulators, *Reviews of Modern Physics* 82 (2010) 3045–3067.
- [17] J. E. Moore, The birth of topological insulators, *Nature* 464 (2010) 194–198.
- [18] F. D. M. Haldane, S. Raghu, Possible Realization of Directional Optical Waveguides in Photonic Crystals with Broken Time-Reversal Symmetry, *Physical Review Letters* 100 (2008) 013904.
- [19] Z. Wang, Y. Chong, J. D. Joannopoulos, M. Soljačić, Observation of unidirectional backscattering-immune topological electromagnetic states, *Nature* 461 (2009) 772–775.
- [20] L.-H. Wu, X. Hu, Scheme for achieving a topological photonic crystal by using dielectric material, *Physical review letters* 114 (2015) 223901.

- [21] F. Gao, H. Xue, Z. Yang, K. Lai, Y. Yu, X. Lin, Y. Chong, G. Shvets, B. Zhang, Topologically protected refraction of robust kink states in valley photonic crystals, *Nature Physics* 14 (2018) 140–144.
- [22] M. Xiao, G. Ma, Z. Yang, P. Sheng, Z. Zhang, C. T. Chan, Geometric phase and band inversion in periodic acoustic systems, *Nature Physics* 11 (2015) 240–244.
- [23] Z. Yang, F. Gao, X. Shi, X. Lin, Z. Gao, Y. Chong, B. Zhang, Topological Acoustics, *Physical Review Letters* 114 (2015) 114301.
- [24] A. B. Khanikaev, R. Fleury, S. H. Mousavi, A. Alu, Topologically robust sound propagation in an angular-momentum-biased graphene-like resonator lattice, *Nature communications* 6 (2015) 1–7.
- [25] C. He, X. Ni, H. Ge, X.-C. Sun, Y.-B. Chen, M.-H. Lu, X.-P. Liu, Y.-F. Chen, Acoustic topological insulator and robust one-way sound transport, *Nature physics* 12 (2016) 1124–1129.
- [26] J. Lu, C. Qiu, L. Ye, X. Fan, M. Ke, F. Zhang, Z. Liu, Observation of topological valley transport of sound in sonic crystals, *Nature Physics* 13 (2017) 369–374.
- [27] Y. Ding, Y. Peng, Y. Zhu, X. Fan, J. Yang, B. Liang, X. Zhu, X. Wan, J. Cheng, Experimental Demonstration of Acoustic Chern Insulators, *Physical Review Letters* 122 (2019) 014302.
- [28] P. Gao, Z. Zhang, J. Christensen, Sonic valley-Chern insulators, *Physical Review B* 101 (2020) 020301.
- [29] D. Torrent, D. Mayou, J. Sánchez-Dehesa, Elastic analog of graphene: Dirac cones and edge states for flexural waves in thin plates, *Physical Review B* 87 (2013) 115143.
- [30] S. H. Mousavi, A. B. Khanikaev, Z. Wang, Topologically protected elastic waves in phononic metamaterials, *Nature communications* 6 (2015) 1–7.
- [31] R. Chaunsali, C.-W. Chen, J. Yang, Subwavelength and directional control of flexural waves in zone-folding induced topological plates, *Physical Review B* 97 (2018) 054307.

- [32] M. Miniaci, R. K. Pal, B. Morvan, M. Ruzzene, Experimental Observation of Topologically Protected Helical Edge Modes in Patterned Elastic Plates, *Physical Review X* 8 (2018) 031074.
- [33] M. Yan, J. Lu, F. Li, W. Deng, X. Huang, J. Ma, Z. Liu, On-chip valley topological materials for elastic wave manipulation, *Nature Materials* 17 (2018) 993–998.
- [34] H. Chen, H. Nassar, G. Huang, A study of topological effects in 1D and 2D mechanical lattices, *Journal of the Mechanics and Physics of Solids* 117 (2018) 22–36.
- [35] Y. Chen, X. Liu, G. Hu, Topological phase transition in mechanical honeycomb lattice, *Journal of the Mechanics and Physics of Solids* 122 (2019) 54–68.
- [36] W. Zhou, B. Wu, Z. Chen, W. Chen, C. W. Lim, J. N. Reddy, Actively controllable topological phase transition in homogeneous piezoelectric rod system, *Journal of the Mechanics and Physics of Solids* 137 (2020) 103824.
- [37] Y. Zhao, X. Zhou, G. Huang, Non-reciprocal Rayleigh waves in elastic gyroscopic medium, *Journal of the Mechanics and Physics of Solids* 143 (2020) 104065.
- [38] L.-Y. Zheng, G. Theocharis, R. Fleury, V. Tournat, V. Gusev, Tilted double Dirac cone and anisotropic quantum-spin-Hall topological insulator in mechanical granular graphene, *New Journal of Physics* 22 (2020) 103012.
- [39] L. Yang, K. Yu, B. Bonello, B. Djafari-Rouhani, W. Wang, Y. Wu, Abnormal topological refraction into free medium at subwavelength scale in valley phononic crystal plates, *Physical Review B* 103 (2021) 184303.
- [40] Y. Chen, J. Li, J. Zhu, Topology optimization of quantum spin Hall effect-based second-order phononic topological insulator, *Mechanical Systems and Signal Processing* 164 (2022) 108243.
- [41] W. Wang, Y. Jin, W. Wang, B. Bonello, B. Djafari-Rouhani, R. Fleury, Robust Fano resonance in a topological mechanical beam, *Physical Review B* 101 (2020) 024101.

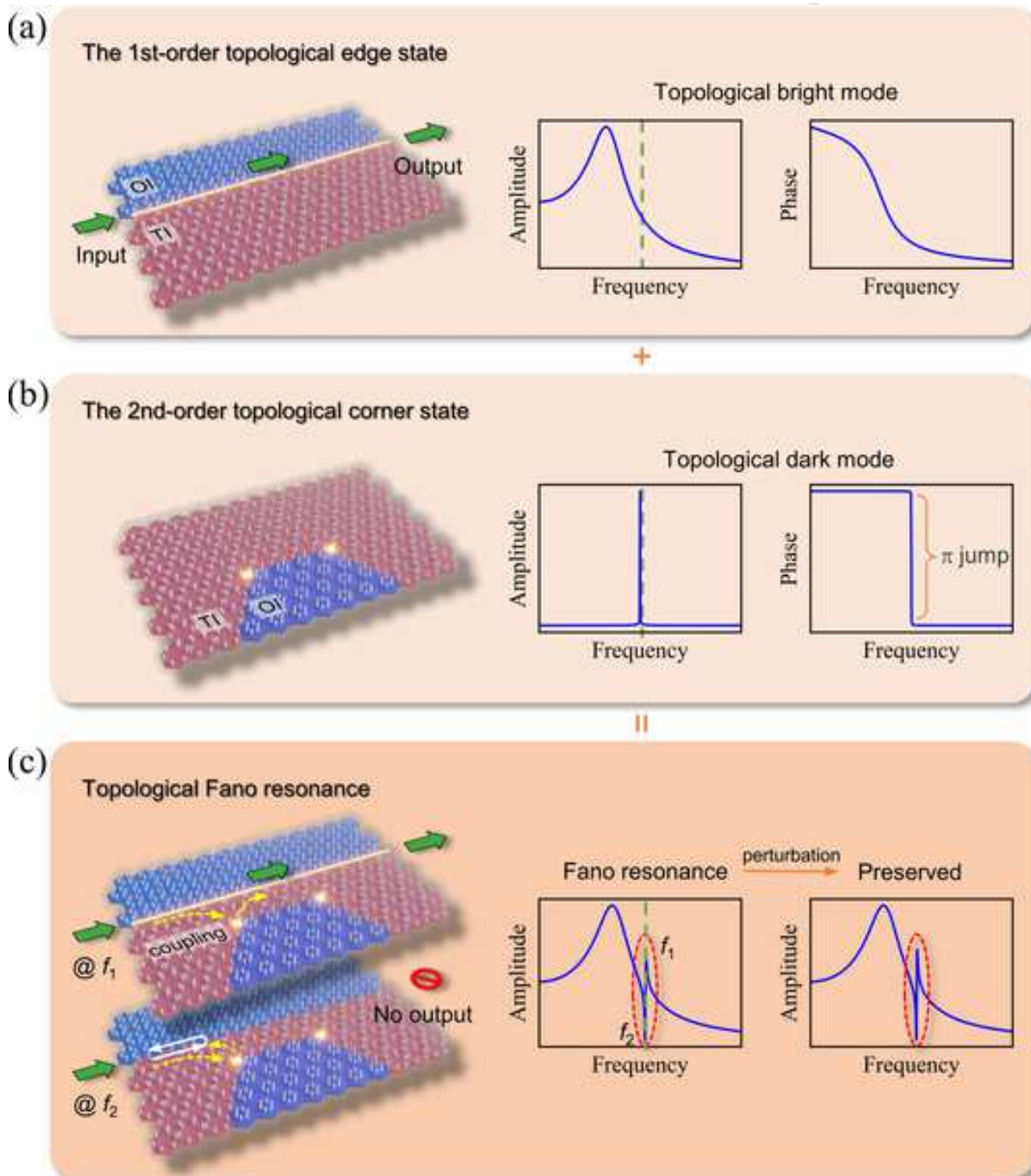
- [42] C.-Y. Ji, G.-B. Liu, Y. Zhang, B. Zou, Y. Yao, Transport tuning of photonic topological edge states by optical cavities, *Physical Review A* 99 (2019) 043801.
- [43] C.-Y. Ji, Y. Zhang, Y. Liao, X. Zhou, J.-H. Jiang, B. Zou, Y. Yao, Fragile topologically protected perfect reflection for acoustic waves, *Physical Review Research* 2 (2020) 013131.
- [44] C.-Y. Ji, Y. Zhang, B. Zou, Y. Yao, Robust Fano resonance in the photonic valley Hall states, *Physical Review A* 103 (2021) 023512.
- [45] A. Benalcazar Wladimir, B. B. Andrei, L. Hughes Taylor, Quantized electric multipole insulators, *Science* 357 (2017) 61–66.
- [46] W. A. Benalcazar, B. A. Bernevig, T. L. Hughes, Electric multipole moments, topological multipole moment pumping, and chiral hinge states in crystalline insulators, *Phys. Rev. B* 96 (2017) 245115.
- [47] M. Serra-Garcia, V. Peri, R. Süsstrunk, O. R. Bilal, T. Larsen, L. G. Villanueva, S. D. Huber, Observation of a phononic quadrupole topological insulator, *Nature* 555 (2018) 342–345.
- [48] C. W. Peterson, W. A. Benalcazar, T. L. Hughes, G. Bahl, A quantized microwave quadrupole insulator with topologically protected corner states, *Nature* 555 (2018) 346–350.
- [49] S. Mittal, V. V. Orre, G. Zhu, M. A. Gorlach, A. Poddubny, M. Hafezi, Photonic quadrupole topological phases, *Nature Photonics* 13 (2019) 692–696.
- [50] J. Noh, W. A. Benalcazar, S. Huang, M. J. Collins, K. P. Chen, T. L. Hughes, M. C. Rechtsman, Topological protection of photonic mid-gap defect modes, *Nature Photonics* 12 (2018) 408–415.
- [51] W. A. Benalcazar, T. Li, T. L. Hughes, Quantization of fractional corner charge in C_n -symmetric higher-order topological crystalline insulators, *Physical Review B* 99 (2019) 245151.
- [52] H. Fan, B. Xia, L. Tong, S. Zheng, D. Yu, Elastic Higher-Order Topological Insulator with Topologically Protected Corner States, *Physical Review Letters* 122 (2019) 204301.

- [53] H. Xue, Y. Yang, F. Gao, Y. Chong, B. Zhang, Acoustic higher-order topological insulator on a kagome lattice, *Nature Materials* 18 (2019) 108–112.
- [54] Z.-Z. Yang, X. Li, Y.-Y. Peng, X.-Y. Zou, J.-C. Cheng, Helical Higher-Order Topological States in an Acoustic Crystalline Insulator, *Physical Review Letters* 125 (2020) 255502.
- [55] B. Xie, G. Su, H.-F. Wang, F. Liu, L. Hu, S.-Y. Yu, P. Zhan, M.-H. Lu, Z. Wang, Y.-F. Chen, Higher-order quantum spin Hall effect in a photonic crystal, *Nature communications* 11 (2020) 1–8.
- [56] Y. Wu, M. Yan, Z.-K. Lin, H.-X. Wang, F. Li, J.-H. Jiang, On-chip higher-order topological micromechanical metamaterials, *Science Bulletin* 66 (2021) 1959–1966.
- [57] C.-W. Chen, R. Chaunsali, J. Christensen, G. Theocharis, J. Yang, Corner states in a second-order mechanical topological insulator, *Communications Materials* 2 (2021) 62.
- [58] S. An, T. Liu, H. Fan, H. Gao, Z. Gu, S. Liang, S. Huang, Y. Zheng, Y. Chen, L. Cheng, J. Zhu, Second-order elastic topological insulator with valley-selective corner states, *International Journal of Mechanical Sciences* 224 (2022) 107337.
- [59] L. Yang, Y. Wang, Y. Meng, Z. Zhu, X. Xi, B. Yan, S. Lin, J. Chen, B.-j. Shi, Y. Ge, S.-q. Yuan, H. Chen, H.-x. Sun, G.-G. Liu, Y. Yang, Z. Gao, Observation of Dirac Hierarchy in Three-Dimensional Acoustic Topological Insulators, *Phys. Rev. Lett.* 129 (2022) 125502.
- [60] B. Xie, H.-X. Wang, X. Zhang, P. Zhan, J.-H. Jiang, M. Lu, Y. Chen, Higher-order band topology, *Nature Reviews Physics* 3 (2021) 520–532.
- [61] L. Yang, K. Yu, Y. Wu, R. Zhao, S. Liu, Topological spin-Hall edge states of flexural wave in perforated metamaterial plates, *Journal of Physics D: Applied Physics* 51 (2018) 325302.
- [62] S.-Y. Yu, C. He, Z. Wang, F.-K. Liu, X.-C. Sun, Z. Li, H.-Z. Lu, M.-H. Lu, X.-P. Liu, Y.-F. Chen, Elastic pseudospin transport for integratable topological phononic circuits, *Nature Communications* 9 (2018) 3072.

- [63] B. Xie, G. Su, H.-F. Wang, F. Liu, L. Hu, S.-Y. Yu, P. Zhan, M.-H. Lu, Z. Wang, Y.-F. Chen, Higher-order quantum spin Hall effect in a photonic crystal, *Nature Communications* 11 (2020) 3768.
- [64] O. C. Zienkiewicz, R. L. Taylor, J. Z. Zhu, *The finite element method: its basis and fundamentals*, Elsevier, Amsterdam, 2005.
- [65] J. Achenbach, *Wave propagation in elastic solids*, Elsevier, Amsterdam, 2012.
- [66] G. Sun, L. Yuan, Y. Zhang, X. Zhang, Y. Zhu, Q-factor enhancement of Fano resonance in all-dielectric metasurfaces by modulating meta-atom interactions, *Scientific Reports* 7 (2017) 8128.
- [67] E. Miranda Jr., E. Nobrega, S. Rodrigues, C. Aranas Jr., J. Dos Santos, Wave attenuation in elastic metamaterial thick plates: Analytical, numerical and experimental investigations, *International Journal of Solids and Structures* 204-205 (2020) 138–152.
- [68] R. Chaunsali, C.-W. Chen, J. Yang, Experimental demonstration of topological waveguiding in elastic plates with local resonators, *New Journal of Physics* 20 (2018) 113036.
- [69] K.-H. O, K.-H. Kim, Ultrahigh-Q Fano resonance using topological corner modes in second-order pseudospin-hall photonic systems, *Optics & Laser Technology* 147 (2022) 107616.

The edge and the corner states are investigated by a weak form for elastic wave equations
Topological Fano interaction is formulated by combining the edge and the corner states
Fano resonance features a unique advantage of robustness against geometrical imperfections

Journal Pre-proof



Ying Wu, Linyun Yang: Conceptualization, Methodology, Software. **Linyun Yang, Ying Wu:** Data curation, Writing- Original draft preparation. **Linyun Yang:** Visualization, Investigation. **Ying Wu, Kaiping Yu:** Supervision. **Rui Zhao:** Validation. **Ying Wu, Kaiping Yu, Rui Zhao, Wei Wang, Bernard Bonello, Bahram Djafari-Rouhani:** Writing- Reviewing and Editing.

Declaration of interests

The authors declare that they have no known competing financial interests or personal relationships that could have appeared to influence the work reported in this paper.

The authors declare the following financial interests/personal relationships which may be considered as potential competing interests:

Journal Pre-proof